Cold-formed stainless steel CHS beam-columns – testing, simulation and design

Craig Buchanan[a,*], Ou Zhao[b], Esther Real[c], Leroy Gardner[a]

[a]*Department of Civil and Environmental Engineering, Imperial College London, London, UK*
[b]*School of Civil and Environmental Engineering, Nanyang Technological University, Singapore*
[c]*Department of Civil and Environmental Engineering, Universitat Politècnica de Catalunya, Barcelona, Spain*

Abstract

The present work was prompted by shortcomings identified in existing design provisions for stainless steel circular hollow section (CHS) beam-columns. First, addressing a lack of existing experimental data, a series of ferritic stainless steel CHS beam-column tests was undertaken at the cross-section and member levels. In total, 26 beam-column tests, including two section sizes (a non-slender class 3 and slender class 4 cross-section), two member slenderness values for each cross-section type and a wide range of loading eccentricities were carried out to investigate the interaction between local and global buckling. Following validation of finite element (FE) models, a numerical study was then undertaken to explore the buckling response of stainless steel CHS beam-columns, covering austenitic, duplex and ferritic grades with a wide range of local and global slendernesses and applied loading eccentricities. Over 2000 numerical results were generated and used to assess new design proposals for stainless steel beam-columns, featuring improved compression and bending end points and new interaction factors. The new proposals are more consistent and more accurate in their resistance predictions than the current EN 1993-1-4 (2015) design approach. The reliability of the new proposals has been verified by means of statistical analyses according to EN 1990 (2005).

Keywords: beam-columns, combined loading, circular hollow sections, design methods, experiments, finite element modelling, stainless steel

1. Introduction

Stainless steel offers an appealing combination of mechanical and physical properties, including high ductility, stiffness and strength, corrosion resistance, recyclability and aesthetics. The use of stainless steel in the construction sector is anticipated to increase with a greater emphasis on sustainability. Iron alloys, with corrosion resistance properties and a minimum

*Corresponding author
Email address: craig.buchanan08@imperial.ac.uk (Craig Buchanan)

10.5% chromium content, are denoted as stainless steels [3]. The most common types of stainless steel in construction are austenitic, duplex and ferritic, and these are included in the European structural design standard EN 1993-1-4 (2015). The austenitic grades are the most prevalent, duplex grades offer improved mechanical and corrosion resistant properties at a higher cost, while ferritic grades have the lowest and most stable cost, but with reduced corrosion resistance [4]. Ferritic grades are anticipated to become more common in construction due to their lower, more stable cost, which is the result of a reduced chromium and nickel content. Circular hollow sections (CHS) are a common structural element and are popular due to their aesthetics and advantageous properties over other open and closed cross-sections. CHS offer high torsional resistance, the ability to be filled with concrete to act as composite members, reduced drag loading in a fluid, good bi-axial bending resistance and reduced maintenance requirements with a smaller exposed external area, compared with alternative cross-sections [5]. The increasing use of stainless steel and the popularity of CHS necessitates safe, efficient and reliable design rules for stainless steel CHS.

In recent years a significant number of experiments on stainless steel CHS structural elements have been reported in the literature. At the cross-section level stub column tests have been undertaken on austenitic [6–15], duplex [12, 15–17] and ferritic [15, 18] stainless steel CHS and beam tests have been carried out on austenitic [7, 19–21] and duplex [20, 21] stainless steel CHS. The test results have shown that the EN 1993-1-4 (2015) cross-section capacity predictions are overly conservative, particularly for stocky cross-sections. The continuous strength method (CSM) has been extended to cover metallic CHS and facilitate more accurate and consistent predictions of cross-section resistance [22].

Flexural buckling tests on austenitic stainless steel CHS columns have been reported for members with pin-ended conditions [6, 7, 20, 23] and fixed-ended conditions [9]. Shortcomings in the current EN 1993-1-4 (2015) member stability design provisions have also been observed, with unconservative resistance predictions for intermediate global slenderness values [15, 24, 25]. An experimental and numerical study was recently undertaken on cold-formed austenitic, duplex and ferritic CHS columns and a new safe and efficient flexural buckling curve for was proposed [15]. New flexural buckling curves for hot-finished stainless steel CHS were also recommended in a parallel numerical study [26].

Resistance predictions for stainless steel CHS under combined axial loading and bending moment at the cross-section level are provided in EN 1993-1-4 (2015), though limited experimental data are available for this loading scenario. Zhao et al. [14] reported combined axial loading and bending moment tests on austenitic stainless steel CHS and undertook a parallel finite element study [27]. The experimental and numerical results were compared with the EN 1993-1-4 (2015) design provisions; these were again found to be overly conservative and new design rules utilising the continuous strength method (CSM) end points and a nonlinear interaction curve were proposed [27]. Similar studies have been undertaken on square hollow sections (SHS) and rectangular hollow sections (RHS) at the local level, with combined loading tests on ferritic stainless steel grades reported in [28, 29]; current design

standard resistance predictions were noted to be overly conservative, whereas the CSM was shown to provide accurate capacity predictions.

Experiments on stainless steel CHS beam-column members have been undertaken for austenitic stainless steel grades [6, 20, 23] and it has been demonstrated that current EN 1993-1-4 (2015) design rules transition from overly conservative to unconservative as the applied load varies from pure bending towards pure compression [23]. SHS and RHS beam-column tests have been undertaken for austenitic grades [6, 30], for duplex grades [31, 32] and for ferritic grades [33, 34]. These studies have noted shortcomings in existing international design standards for stainless steel beam-column resistance predictions; existing test data, supplemented with additional numerical simulations, have been used to propose improvements [35, 36].

It is apparent from the literature that there are limited experimental data for stainless steel CHS elements under combined axial loading and bending moment at the cross-section level and for beam-columns at the member level. The aim of this study is to produce experimental data on ferritic stainless steel CHS at both of the aforementioned structural levels, to generate additional data numerically, to further evaluate the current design provisions in EN 1993-1-4 (2015) and then to develop efficient and reliable design rules for stainless steel CHS beam-columns.

2. Experiments

2.1. General overview

The experimental investigation consisted of material tests, stub column tests, cross-section level combined axial loading and bending moment tests and member level beam-column tests on grade EN 1.4512 ferritic stainless steel CHS elements. The tested CHS were produced by cold-forming and laser welding and their chemical composition, as listed in the mill certificates, is reported in Table 1. Two different CHS cross-sections were tested, with both close to the class 3 slenderness limit in compression – a class 3 80×1.5 CHS ($D/(t\varepsilon^2) = 89.1$) and a class 4 101.6×1.5 CHS ($D/(t\varepsilon^2) = 102.7$), according to the EN 1993-1-4 (2015) compressive class 3 limit of $D/(t\varepsilon^2) = 90$, where D is the CHS outer diameter, t is the wall thickness and $\varepsilon^2 = \left(\frac{235}{\sigma_{0.2}}\frac{E}{210000}\right)$, with E being the Young's modulus and $\sigma_{0.2}$ being the yield (0.2% proof) strength of the material. EN 1993-1-4 (2015) does not include guidance for the classification of CHS under combined loading, and hence linear interpolation between the compressive ($D/(t\varepsilon^2) = 90$) and bending ($D/(t\varepsilon^2) = 280$) class 3 limits was utilised, as discussed later in Section 4.1. As a consequence, the eccentrically loaded specimens that were class 4 under pure compression became class 3 under combined compression and bending. The material property tests were carried out at Imperial College London (ICL), whereas the cross-section and member level tests were undertaken at Universitat Politècnica de Catalunya (UPC). The specimen notation adopted for the cross-section and member tests is described by

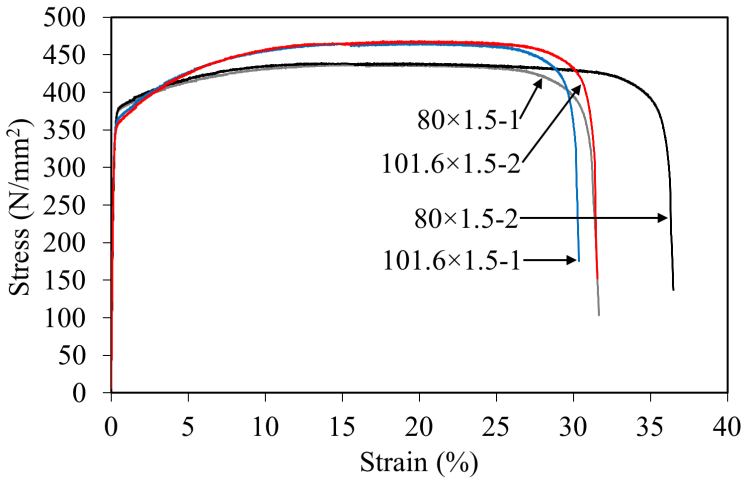

Figure 1: Measured tensile coupon stress-strain curves [15]

means of the following example: the 80×1.5-450-P-10E specimen is an 80×1.5 mm CHS cross-section with a 450 mm effective length (or nominal length for the stub columns); 'P' denotes pin-ended conditions (or 'F' fixed ended conditions for the stub columns) and '-10E' indicates an eccentrically loaded specimen with '10' being the nominal eccentricity in mm; repeat stub column specimens end with an 'R'.

Section	C (%)	Si (%)	S (%)	P (%)	Mn (%)	Cr (%)	Ni (%)	Mo (%)	Ti (%)	N (%)	Co (%)
80×1.5	0.011	0.46	0.010	0.024	0.27	11.68	0.25	0.04	0.22	0.008	0.01
101.6×1.5	0.016	0.44	0.001	0.026	0.28	11.55	-	-	0.24	0.012	-

Table 1: Chemical composition of grade EN 1.4512 ferritic stainless steel material from the mill certificate

2.2. Material properties

Tensile coupon tests were undertaken to measure the inherent material properties of the tested ferritic stainless steel CHS specimens; these tests have been fully reported by Buchanan et al. [15].

Measured stress-strain curves from the tensile coupons are provided in Figure 1. The Young's modulus E, 0.2% proof stress $\sigma_{0.2}$, 1.0% proof stress $\sigma_{1.0}$, ultimate tensile stress σ_{u}, strain at the ultimate tensile stress ε_{u}, fracture strain over the marked gauge length ε_{f}, the Ramberg-Osgood parameter n [37] and the extended parameters $m_{1.0}$ (previously referred to as $n'_{0.2,1.0}$) and m_{u} (previously referred to as $n'_{0.2,\mathrm{u}}$) [38–41] determined from the coupon tests, are listed in Table 2.

Coupon	E (N/mm^2)	$\sigma_{0.2}$ (N/mm^2)	$\sigma_{1.0}$ (N/mm^2)	σ_{u} (N/mm^2)	ε_{u} (%)	ε_{f} (%)	n	$m_{1.0}$	m_{u}
80×1.5-1	229400	369	385	437	19.4	41.5	8.4	1.6	1.8
80×1.5-2	214700	373	388	439	13.7	47.1	9.0	1.6	1.7
101.6×1.5-1	227500	361	378	466	18.5	43.1	15.4	2.4	1.7
101.6×1.5-2	221100	355	373	468	19.4	45.5	13.5	2.4	1.7

Table 2: Summary of the tensile coupon material properties [15]

2.3. Geometric properties

The geometric properties of the specimens were determined prior to testing. The short combined loading and long beam-column specimens were welded to 10 mm thick end plates for mechanical attachment to the knife edges; the geometric properties of these specimens were measured after the welding. The outer diameter was measured at three equally spaced longitudinal locations for the stub columns and short pin-ended columns ($L \leq 500$ mm), and at five equally spaced longitudinal locations for the remaining longer beam-column specimens. At each longitudinal measurement location the outer diameter was recorded in four evenly distributed orientations (at 45° intervals) with mechanical callipers, allowing the average outer diameter D of the specimen and the EN 10219-2 (2006) 'out-of-roundness' O to be determined. The maximum measured 'out-of-roundness' was $O = 1.9\%$ which is marginally less than the codified limit of $O \leq 2\%$. The average wall thickness t was determined by measuring the wall thickness at eight equally spaced locations (at 45° intervals) around the circumference at the tube ends, and in accordance with EN 10219-2 (2006) at a distance not less than $2t$ from the weld location. The wall thicknesses of the short combined loading and long beam-column specimens could not be measured prior to testing due to the welded end plates; however, the thickness variation around the ferritic stub columns was small ($< 4.5\%$, < 0.06 mm) and the average wall thickness t for the ferritic stub columns was therefore used for the eccentrically loaded specimens. The average specimen length L, which for the pin-ended members includes the additional length from the end plates and knife edges, was determined based on measurements taken at 90° equally spaced locations around the circumference of the CHS using a tape measure. The mid-point global imperfections ω_0 were recorded by measuring the deviation from a flat plane linking the two ends of the specimens, which was achieved using an aluminium extrusion that was placed over the end plates and the deviation measured using mechanical callipers. For the stub columns this deviation was measured using the bottom of a spirit level and feeler gauges. For the pin-ended specimens, the imperfection measurements were undertaken on the two faces parallel to the knife-edge axis, to obtain the imperfection in the direction of buckling. The average geometric properties of the specimens are provided in Table 3 for the stub columns, Tables 5 and 6 for the short combined loading specimens and Tables 7 and 8 for the beam-columns. The position of the weld for the eccentrically loaded specimens was kept constant, with the weld orientated to be on the least compressed face.

2.4. Stub column tests

Stub column tests were carried out to ascertain the cross-sectional load-carrying capacity under pure compression and to determine compressive material properties. The stub column tests have again been comprehensively reported by Buchanan et al. [15].

The average outer diameter D, wall thickness t, length L and initial global imperfection ω_0, along with the ultimate axial load N_{u}, corresponding true end shortening at the ultimate load δ_{u}, accounting for the deformation of the end platens [11, 43], and ultimate load normalised by the yield load $N_{\mathrm{u}}/A\sigma_{0.2}$ are reported in Table 3. The ultimate axial loads N_{u} were very close to the yield load $A\sigma_{0.2}$, highlighting that the cross-sections are all close to the class 3 slenderness limit in compression. The compressive material properties derived from the stub column tests up to the compressive 0.2% proof stress, which were deemed not to be influenced by local buckling since the peak of the stress-strain curve occurred beyond this point, (E_{stub}, $\sigma_{0.2,\mathrm{stub}}$ and n_{stub} determined using the same techniques as the tensile coupon material properties) are listed in Table 4. The compressive material properties are used in Section 3 for the finite element model validation and subsequent parametric study. The load end-shortening curves are shown in Figure 2, with solid and dashed lines used to distinguish between curves that are in close proximity. The consistent failure mode was the classic 'elephant's foot' buckle at one end of the specimen.

Stub column	D (mm)	t (mm)	L (mm)	ω_0 (mm)	N_{u} (kN)	δ_{u} (mm)	$N_{\mathrm{u}}/A\sigma_{0.2}$
80×1.5-350-F	80.00	1.34	350	0.05	126.7	2.41	1.03
80×1.5-350-FR	80.00	1.34	350	0.15	125.4	2.25	1.02
101.6×1.5-400-F	101.75	1.33	400	0.40	148.5	2.18	0.99
101.6×1.5-400-FR	101.80	1.34	400	0.25	147.2	2.31	0.97

Table 3: Summary of measured geometric properties and test results for stub columns

Specimen	E_{stub} (N/mm^2)	$\sigma_{0.2,\mathrm{stub}}$ (N/mm^2)	n_{stub}	$\sigma_{0.2}/\sigma_{0.2,\mathrm{stub}}$	EN 1993-1-4 (2015) compressive class
80×1.5-350-F	219600	361	5.1	1.03	3
80×1.5-350-FR	217900	359	5.1	1.03	3
101.6×1.5-400-F	218400	341	5.7	1.05	4
101.6×1.5-400-FR	220700	333	5.5	1.07	4

Table 4: Summary of stub column material properties

2.5. Combined axial loading and bending moment test setup

Combined axial loading and bending moment tests on short members were undertaken to determine the cross-sectional resistance under combined loading. Applied load eccentricities

varying from 5 mm to 130 mm were employed to produce a wide range of axial load to bending moment combinations. The length of the specimens was the same as that of the stub columns, but with an additional 10 mm thick carbon steel end plate welded to each end. The end plates were then bolted to knife edges to create pin-ended conditions. An Instron 8805 testing machine was used for these tests, with the test setup shown in Figure 3. A spherical head was employed to ensure full contact between the specimen and the testing machine. The specimens were loosely bolted to the spherical head, an installation load of 5 kN applied and then the end plate and spherical head bolts were tightened, before the removal of the installation load.

The applied load was measured using a load cell incorporated within the testing machine. The specimen end shortening was recorded using an internal LVDT, inside the testing machine, and separately with an external linear position sensor, spanning between the non-rotating outer female knife edge ends. The maximum and minimum strains from the combined loading were measured using two electrical resistance strain gauges attached to opposite faces at mid-height; these strains are used to calculate the initial applied eccentricity, as outlined in Section 2.7. A laser distance measurement sensor positioned slightly above the strain gauge, due to the need to reflect the laser beam, was used to record the mid-height lateral deflection. Dual axis inclinometers were used to measure the end rotations, monitoring the rotation of the end plates parallel and perpendicular to the knife edge axis. The test parameters were recorded at a frequency of 2 Hz using a HBM MGCplus datalogger and Catman software. Strain visualisation dots were painted onto the specimens to allow for easier tracking of the deformations on the reflective specimen surfaces, and the tests were filmed for later review.

The effective length of the test specimens L was taken as the distance between the knife edges, which were each 40 mm thick, as shown in Figure 3. The global slenderness values were $\overline{\lambda} = 0.21$ for the 80×1.5 CHS and $\overline{\lambda} = 0.17$ for the 101.6×1.5 CHS, calculated using Equations 1 and 2,

$$\overline{\lambda} = \sqrt{\frac{A\sigma_{0.2}L^2}{\pi^2 EI}} \text{ for class 1, 2 and 3 cross-sections} \tag{1}$$

$$\overline{\lambda} = \sqrt{\frac{A_{\text{eff}}\sigma_{0.2}L^2}{\pi^2 EI}} \text{ for class 4 cross-sections} \tag{2}$$

where A is the gross cross-sectional area, A_{eff} is the effective cross-sectional area, $\sigma_{0.2}$ is the 0.2% proof stress, E is the Young's modulus, I is the second moment of area and L is the effective length. EN 1993-1-4 (2015) does not provide an expression for A_{eff} for a CHS and therefore the simplified design formula proposed in [22, 44] was employed, which is an adaptation of the BS 5950-1 (2000) expression accounting for the EN 1993-1-4 (2015) class 3 slenderness limit in compression, as reproduced in Equation 3. The use of A_{eff} (from Equation 3) is recommended up to a local slenderness limit of $D/(t\varepsilon^2) = 250$, and this is due

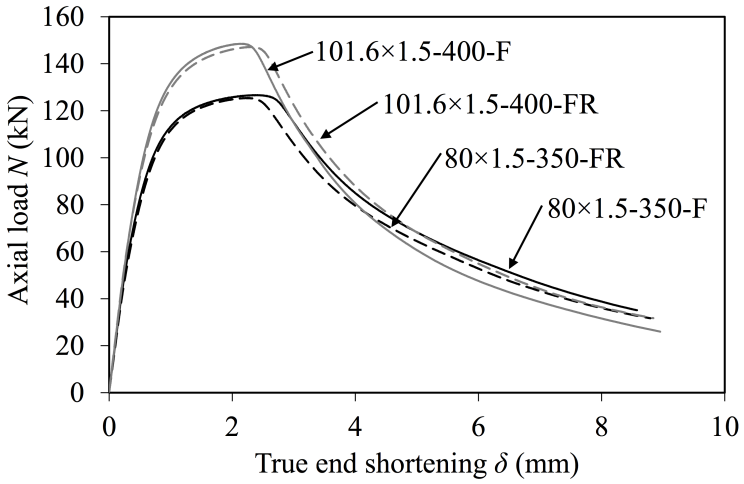

Figure 2: Stub column load end-shortening curves

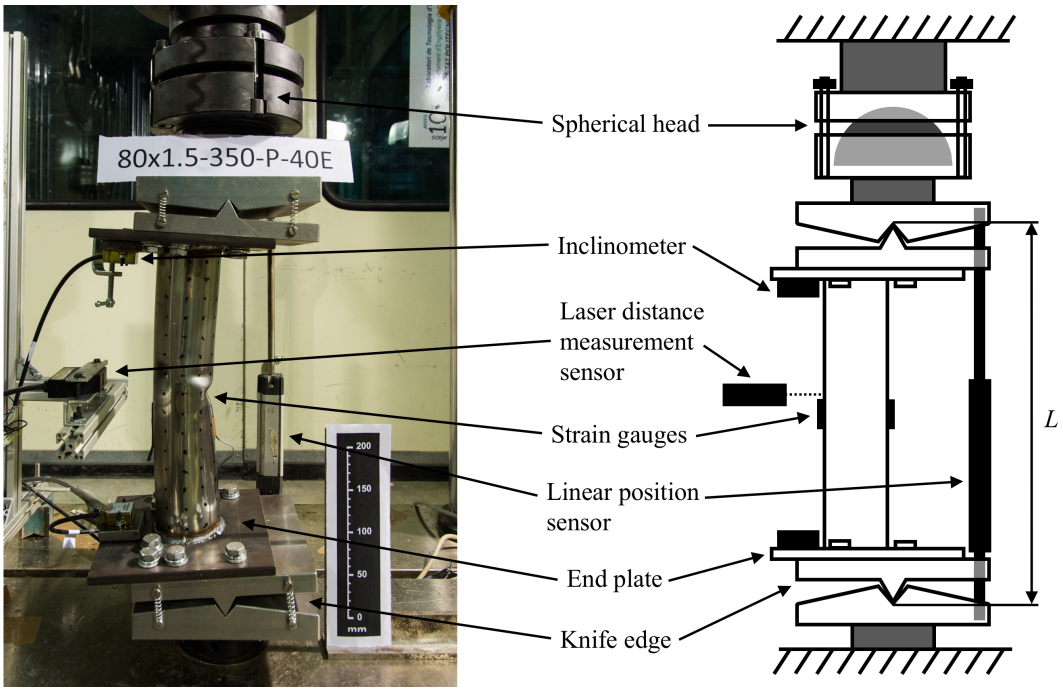

Figure 3: Short beam-column test setup.

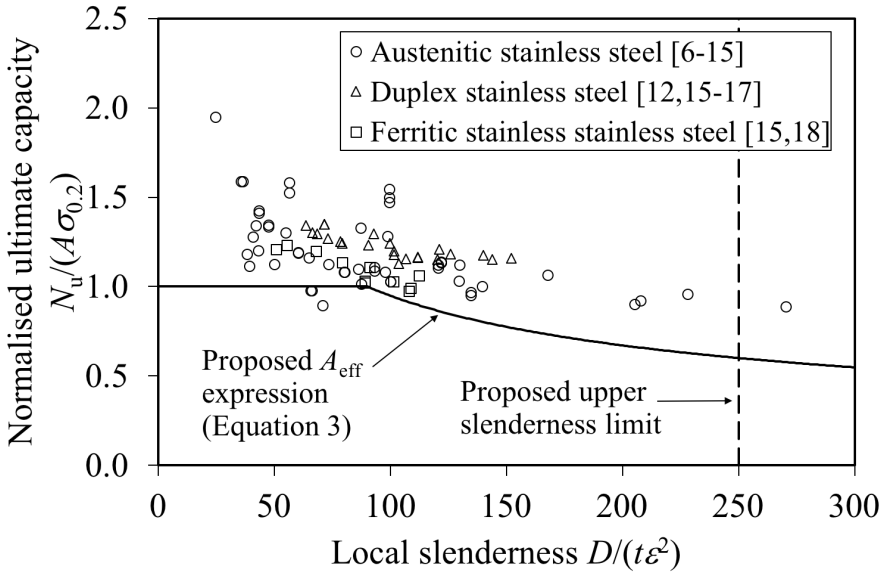

Figure 4: Comparison between proposed effective cross-sectional area A_{eff} equation and existing stainless steel CHS pure compression dataset.

to be included in the next revision of EN 1993-1-4.

$$A_{\text{eff}} = A\left[\left(\frac{90}{D/t}\right)\left(\frac{235}{\sigma_{0.2}}\frac{E}{210000}\right)\right]^{0.5} \tag{3}$$

Similarly, in bending, EN 1993-1-4 (2015) does not provide a design equation for the effective section modulus W_{eff} and an adaptation of the BS 5950-1 (2000) expression accounting for the EN 1993-1-4 (2015) class 3 slenderness limit in bending has been proposed [22], as reproduced in Equation 4, where W_{el} is the elastic section modulus.

$$W_{\text{eff}} = W_{\text{el}}\left[\left(\frac{280}{D/t}\right)\left(\frac{235}{\sigma_{0.2}}\frac{E}{210000}\right)\right]^{0.25} \tag{4}$$

The appropriateness of these effective section property formulations are demonstrated by comparison to the available test data for compression [6–18] and bending [7, 19–21] in Figures 4 and 5 respectively. It is clear from Figure 5 that the proposed expression for the effective section modulus W_{eff} requires further assessment due to the limited existing pure bending stainless steel CHS dataset, and is therefore currently not recommended for code inclusion.

The top platen moved at a displacement rate of 0.2 mm/min, in line with a previous study [14], and the tests were continued beyond the peak load until a knife edge was close to reaching its maximum rotation.

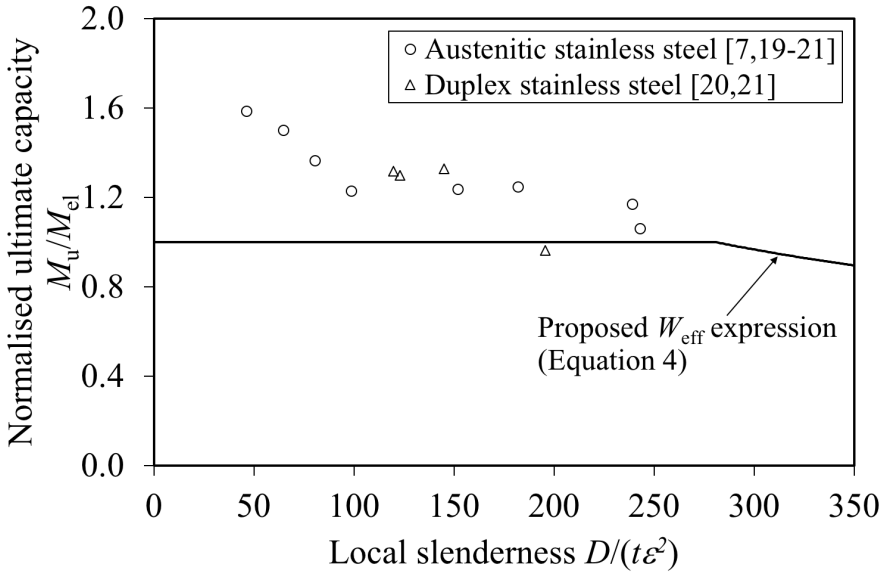

Figure 5: Comparison between the proposed effective section modulus W_{eff} and existing austenitic and duplex stainless steel CHS bending dataset.

2.6. Member beam-column test setup

Member level tests were carried out to examine the beam-column behaviour of ferritic stainless steel CHS elements. The specimens had a nominal effective length of 1600 mm, resulting in global slenderness values of $\overline{\lambda} = 0.74$ for the 80×1.5 CHS and $\overline{\lambda} = 0.56$ for the eccentrically loaded 101.6×1.5 CHS ($\overline{\lambda} = 0.54$ for the concentrically loaded 101.6×1.5-1600-P CHS utilising the proposed effective cross-sectional area A_{eff} under pure compression), calculated again from Equations 1 and 2.

An Ibertest MDA-700 testing machine was used to accommodate the longer test specimens, as shown in Figure 6. No spherical head was used for the long beam-columns due to limited headroom in the testing rig. The test setup was similar to that used for the cross-section level tests described in Section 2.5; the major differences in instrumentation are that the applied load was calculated using pressure gauges and the extension of the loading jack was controlled and recorded using a string potentiometer. A second measure of the end shortening was provided using two additional laser measurement devices monitoring the vertical displacement of the non-rotating female ends of the knife ends. The test parameters were again recorded at 2 Hz and the loading jack moved at a displacement rate of 0.2 mm/min.

2.7. Applied eccentricity

The loading line position was varied to obtain different ratios of axial load to bending moment. The applied eccentricities were determined by both physically measuring the distance from the centre of the specimen to the knife edge loading line and by back-calculating using

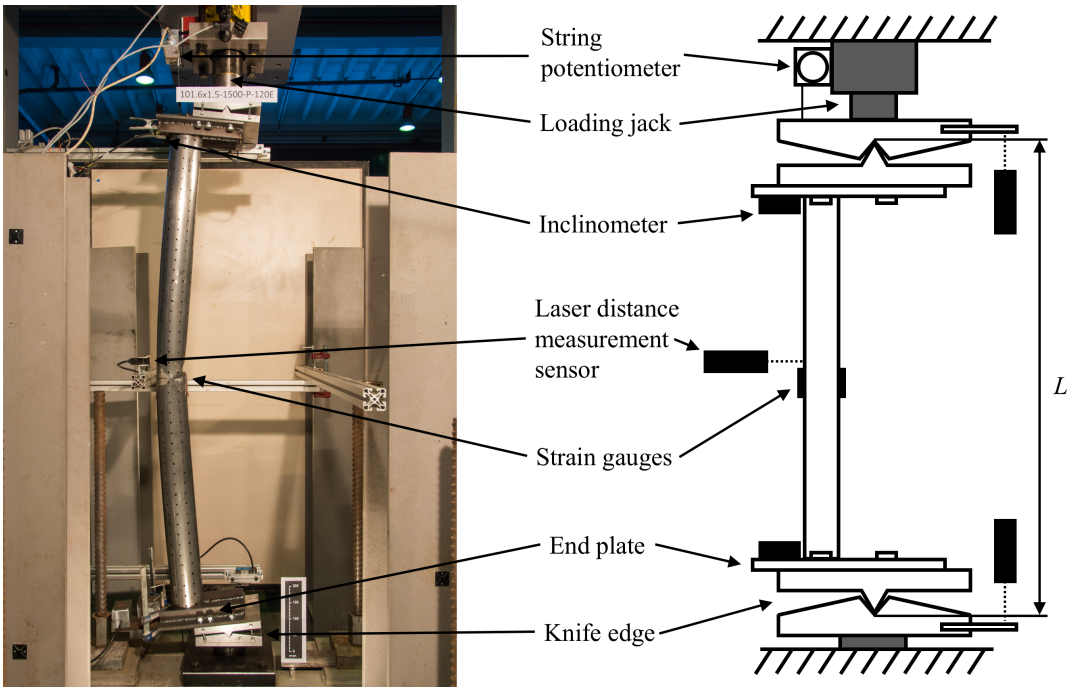

Figure 6: Long beam-column test setup.

the instrumentation readings during the initial elastic loading range. The calculated initial eccentricity e_0 can be determined from

$$e_0 = \frac{EI\left(\varepsilon_{\max} - \varepsilon_{\min}\right)}{DN} - \omega - \omega_0, \tag{5}$$

using the Young's modulus E, second moment of area I, axial load N, average outer diameter D, mid-height lateral displacement ω and the maximum and minimum measured strains $\varepsilon_{\max}$ and $\varepsilon_{\min}$ [14, 32, 46]. Overall the measured eccentricities were reasonably close to those calculated from Equation 5, but the latter are taken to be more accurate [14, 28, 32, 33, 46] and therefore are used in the bending moment calculations. One concentrically loaded column for each cross-section was tested (at both the cross-section and member levels), with the loading eccentricity carefully set such that the sum of the applied eccentricity e_0 and initial global imperfection ω_0 was equal to $L/1000$ to simulate an imperfect column [15].

2.8. Combined axial loading and bending moment test results

The average outer diameter D, wall thickness t, length L, initial global imperfection ω_0, calculated load eccentricity e_0, mid-height deflection at ultimate load ω_{u}, ultimate axial load N_{u}, ultimate mid-height bending moment M_{u} and the average end rotation at ultimate load ϕ_{u} are reported in Tables 5 and 6 for the 80×1.5 and 101.6×1.5 CHS specimens respectively. The ultimate mid-height bending moment M_{u} includes second order effects and was calculated

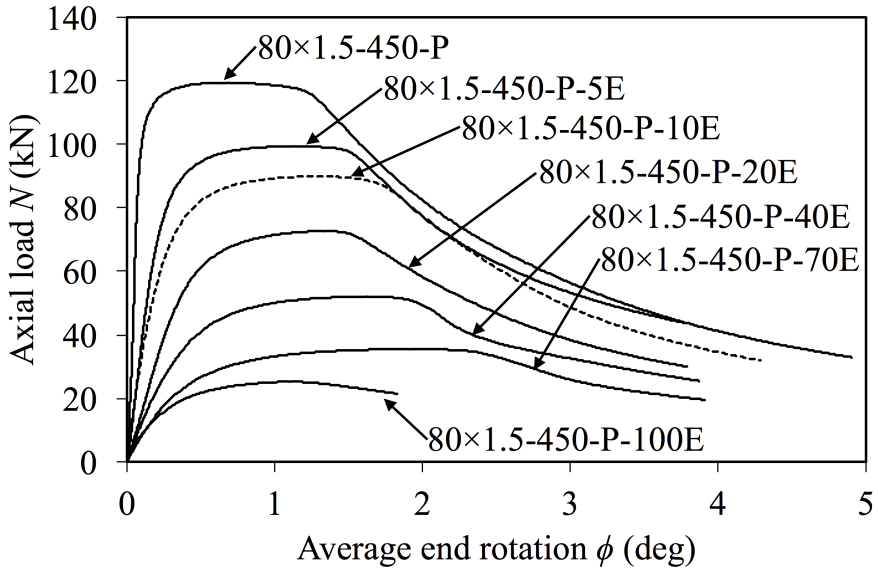

Figure 7: Load–end rotation curves for the 80×1.5 CHS short beam-column specimens.

using

$$M_{\mathrm{u}} = N_{\mathrm{u}} \left(e_0 + \omega_0 + \omega_{\mathrm{u}} \right). \tag{6}$$

Axial load versus average end rotation curves are presented in Figures 7 and 8 for the 80×1.5 and 101.6×1.5 CHS specimens respectively; as with the stub column results presented in Section 2.4, solid and dashed lines are used to distinguish between curves that are in close proximity.

The deformed specimens are shown in Figure 9. Two distinct failure modes were observed, the classical 'elephant's foot' local buckle close to one end of the specimen for the smaller eccentricities and a crumpling local buckle close to the mid-height of the specimen for the larger eccentricities. Poisson's ratio effects were observed for the 101.6×1.5-500-P concentrically loaded CHS specimen, with the painted strain visualisation dots initially moving radially outwards before the specimen started deforming laterally; finite element modelling of stainless steel elliptical hollow sections (EHS) has also shown this behaviour [25].

During the 80×1.5-450-P-100E CHS test it was noticed that the end plates were bending along the last line of bolts and, after the test concluded, yield lines were clearly visible on both end plates. For the remaining short specimens and the untested beam-column specimens stiffening strips were welded along the end plates. In subsequent high eccentricity tests, a small amount of elastic deformation was visible beyond the last line of bolts, though there was no permanent plastic deformation.

Table 5: Summary of the geometric properties and test results for the short 80×1.5 CHS beam-column specimens.

Specimen	D (mm)	t (mm)	L (mm)	ω_0 (mm)	e_0 (mm)	ω_u (mm)	N_u (kN)	M_u (kNm)	ϕ_u (deg)
80×1.5-450-P	80.01	1.34	448.9	0.29	0.11	1.71	119.4	0.25	0.66
80×1.5-450-P-5E	80.03	1.34	449.1	0.18	5.79	2.49	99.4	0.84	1.10
80×1.5-450-P-10E	79.98	1.34	449.4	0.37	8.47	3.02	89.9	1.07	1.33
80×1.5-450-P-20E	79.99	1.34	449.4	0.31	21.63	2.86	72.6	1.80	1.33
80×1.5-450-P-40E	79.99	1.34	449.0	0.22	38.37	3.27	52.0	2.18	1.60
80×1.5-450-P-70E	80.01	1.34	449.1	0.16	71.08	3.75	35.5	2.66	1.89
80×1.5-450-P-100E [a]	80.00	1.34	449.3	0.42	96.99	3.78	25.2	2.55	1.09

Table 6: Summary of the geometric properties and test results for the short 101.6×1.5 CHS beam-column specimens.

Specimen	D (mm)	t (mm)	L (mm)	ω_0 (mm)	e_0 (mm)	ω_u (mm)	N_u (kN)	M_u (kNm)	ϕ_u (deg)
101.6×1.5-500-P	101.68	1.34	499.6	0.13	0.41	2.34	145.4	0.42	0.70
101.6×1.5-500-P-10E	101.76	1.34	499.4	0.45	10.83	2.49	116.0	1.60	0.98
101.6×1.5-500-P-15E	101.76	1.34	499.1	0.44	15.74	2.62	105.4	1.98	0.96
101.6×1.5-500-P-30E	101.69	1.34	499.1	0.14	31.21	2.66	84.8	2.88	1.15
101.6×1.5-500-P-60E	101.71	1.34	498.5	0.19	63.53	2.59	54.6	3.62	1.15
101.6×1.5-500-P-90E	101.71	1.34	498.3	0.28	89.58	2.71	40.9	3.79	1.28
101.6×1.5-500-P-130E	101.68	1.34	498.5	0.31	128.6	3.53	31.5	4.17	1.68

[a] The end plates yielded in bending during this test

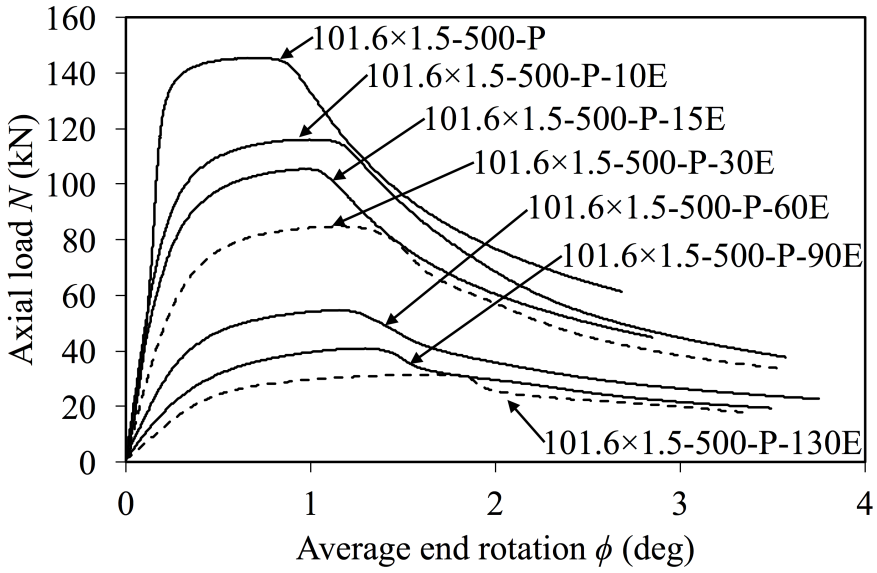

Figure 8: Load–end rotation curves for the 101.6×1.5 CHS short beam-column specimens.

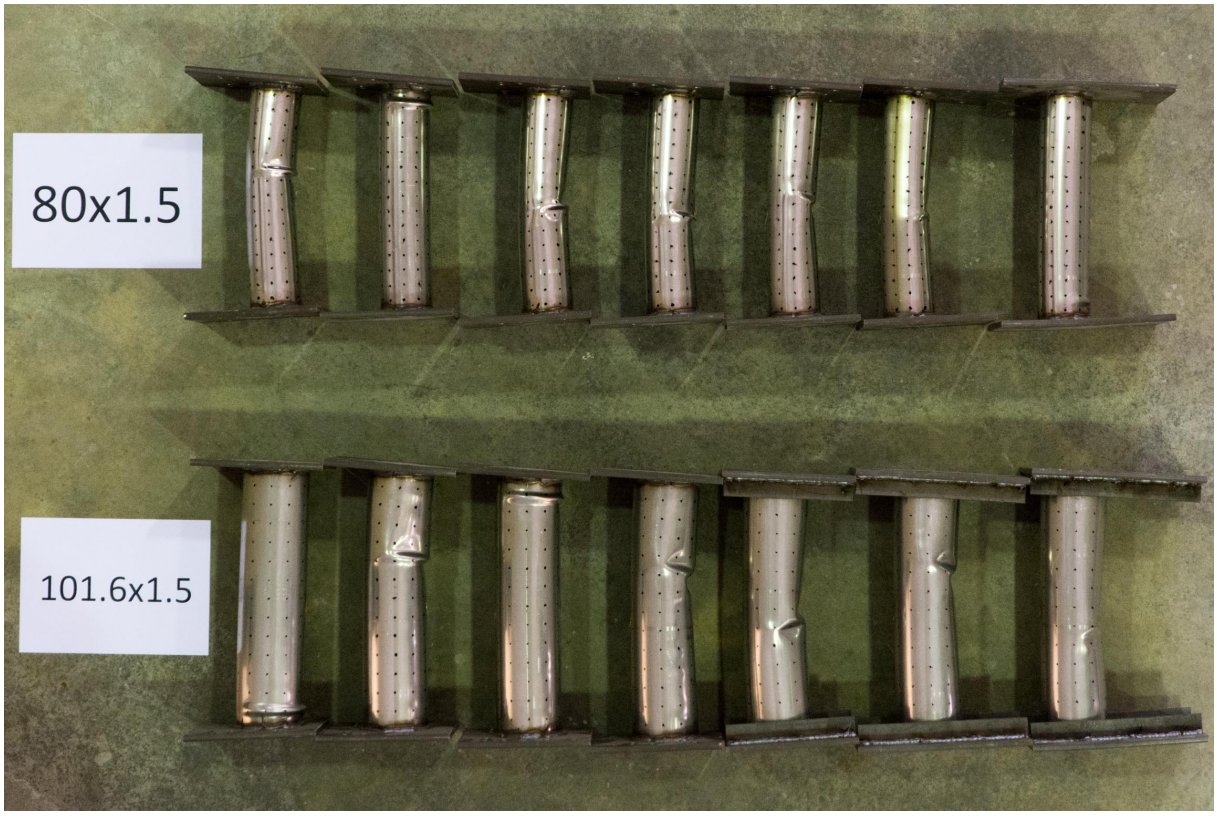

Figure 9: Deformed short beam-columns, with load eccentricity increasing from left to right.

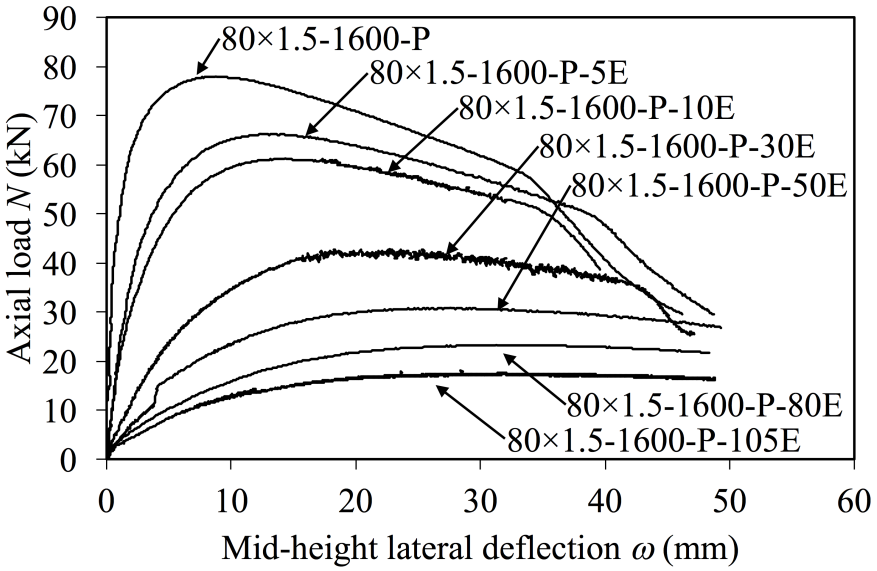

Figure 10: Load–mid height lateral deflection curves for the 80×1.5 CHS long beam-column specimens.

2.9. Member beam-column test results

The average geometric properties and key test results are reported in Tables 7 and 8 for the 80×1.5 and 101.6×1.5 CHS beam-columns, with the same notation as used previously in Section 2.8. Axial load mid-height lateral deflection curves are presented in Figures 10 and 11. The failure mode of the specimens was global flexural buckling, followed by a mid-height local buckle during the post peak unloading for the 101.6×1.5 CHS specimens and all but the two most eccentrically loaded 80×1.5 CHS specimens. The deformed specimens are shown in Figures 12 and 13. The 80×1.5-1600-P-30E CHS specimen was the first member tested, and hence the load mid-height lateral deflection curve has a greater degree of variation as the loading jack displacement control parameters were refined based on this test.

3. Numerical modelling

3.1. Overview

Finite element (FE) models of eccentrically loaded stainless steel CHS were developed and are reported in this section. Abaqus/CAE 2016 [47] was used to perform geometrically and materially nonlinear analyses with imperfections (GMNIA). A validation study was first carried out against the tests performed in Section 2 to confirm the accuracy of the models and to determine the most suitable material stress-strain curve and imperfection amplitudes to employ. A parametric study was then undertaken, with the cross-section and member slenderness, applied loading eccentricity and the type of stainless steel varied in order to generate further data to underpin the development of new design rules.

Table 7: Summary of the geometric properties and test results for the long 80×1.5 CHS beam-column specimens.

Specimen	D (mm)	t (mm)	L (mm)	ω_0 (mm)	e_0 (mm)	ω_u (mm)	N_u (kN)	M_u (kNm)	ϕ_u (deg)
80×1.5-1600-P	80.00	1.34	1599.3	0.78	0.96	8.69	77.9	0.81	1.10
80×1.5-1600-P-5E	80.01	1.34	1599.1	0.84	5.34	12.57	66.3	1.24	1.53
80×1.5-1600-P-10E	80.06	1.34	1599.0	0.60	8.09	14.33	61.2	1.41	1.76
80×1.5-1600-P-30E	80.01	1.34	1598.9	0.64	28.23	22.69	42.8	2.21	2.75
80×1.5-1600-P-50E	80.03	1.34	1598.9	0.43	51.63	27.51	30.8	2.45	3.40
80×1.5-1600-P-80E	80.04	1.34	1598.5	0.44	81.02	31.54	23.2	2.63	3.97
80×1.5-1600-P-105E	80.01	1.34	1598.3	0.05	108.49	43.45	18.2	2.76	3.73

Table 8: Summary of the geometric properties and test results for the long 101.6×1.5 CHS beam-column specimens.

Specimen	D (mm)	t (mm)	L (mm)	ω_0 (mm)	e_0 (mm)	ω_u (mm)	N_u (kN)	M_u (kNm)	ϕ_u (deg)
101.6×1.5-1600-P	101.71	1.34	1599.3	0.85	0.88	8.39	104.1	1.05	1.17
101.6×1.5-1600-P-10E	101.67	1.34	1599.1	0.62	10.68	11.57	88.0	2.01	1.48
101.6×1.5-1600-P-40E	101.73	1.34	1599.1	0.78	38.82	20.71	54.3	3.27	2.53
101.6×1.5-1600-P-70E	101.73	1.34	1598.4	0.63	67.08	24.51	38.7	3.57	3.20
101.6×1.5-1600-P-120E	101.72	1.34	1597.8	0.89	117.2	25.69	27.4	3.95	3.36

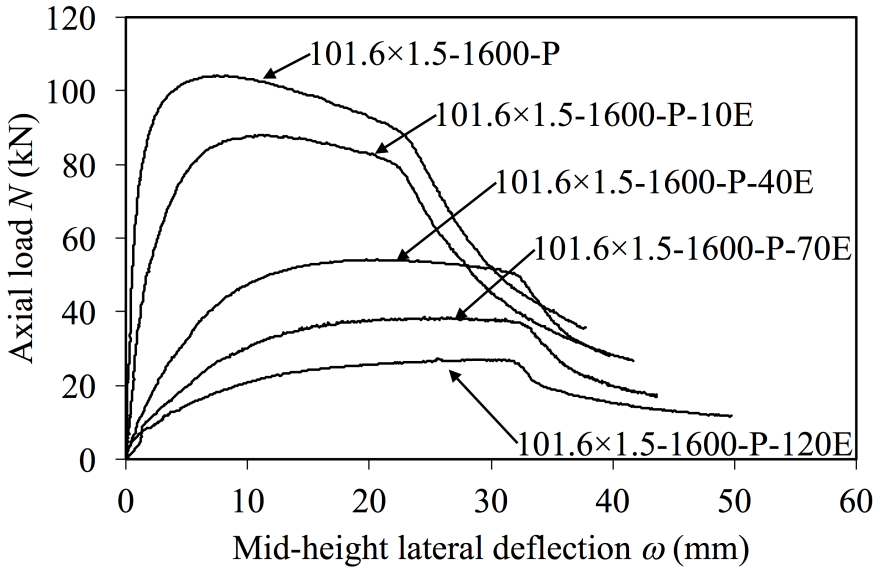

Figure 11: Load–mid height lateral deflection curves for the 101.6×1.5 CHS long beam-column specimens.

Figure 12: Deformed 80×1.5 CHS long beam-columns, with load eccentricity increasing from bottom to top.

Figure 13: Deformed 101.6×1.5 CHS long beam-columns, with load eccentricity increasing from bottom to top.

3.2. Modelling assumptions

The assumptions made in the development of the finite element models are outlined in this section. Previous FE studies of hollow metallic sections [23, 48–50] have used the S4R element, a four-noded doubly curved shell element, with reduced integration, finite membrane strains and six degrees of freedom per node and this was also adopted in this study. The finite element mesh had longitudinal and circumferential dimensions of the wall thickness t, in line with CHS modelling in the literature [14, 23, 27] and a sensitivity study undertaken by Buchanan [51]. Computational efficiency was increased by modelling half of the cross-sections and employing symmetrical boundary conditions. The average outer diameters and wall thicknesses of the tested specimens, reported in Section 2, were used in the finite element models.

Models were built using both tensile and compressive material properties due to the non-symmetric stress-strain response of stainless steel [52]. Compound Ramberg-Osgood material properties [38, 39, 53], calculated from the measured tensile coupons and compressive stub column responses, were used to produce tensile and compressive stress-strain relationships. The compressive relationships, calculated from the stub column tests, include the influence of local buckling and consequently the curve was extrapolated, beyond the onset of local buckling, in parallel with the measured tensile stress-strain curve up to the ultimate tensile material stress σ_{u}. A similar approach has been adopted in other numerical modelling studies [15, 54]. The two material property relationships were inputted into Abaqus/CAE 2016 [47] as true stress and plastic strain. The true stress σ_{true} was calculated as follows,

$$\sigma_{\mathrm{true}} = \sigma_{\mathrm{nom}}(1 + \varepsilon_{\mathrm{nom}}) \tag{7}$$

where σ_{nom} is the nominal engineering stress and $\varepsilon_{\mathrm{nom}}$ is the nominal engineering strain, and the plastic strain $\varepsilon_{\mathrm{plastic}}$ was determined from,

$$\varepsilon_{\mathrm{plastic}} = \ln(1 + \varepsilon_{\mathrm{nom}}) - \frac{\sigma_{\mathrm{true}}}{E} \tag{8}$$

where E is the Young's modulus. For converting the compressive material properties from engineering to true values the nominal engineering strains $\varepsilon_{\mathrm{nom}}$ were input as negative values in Equations 7 and 8.

Prior studies have concluded that the effect of membrane residual stresses in cold-formed tubular sections is small and that they can be safely neglected [6, 55]. The through thickness residual stresses are, however, larger and therefore need to be considered, but the effect of these is implicitly incorporated by utilising measured material properties. The adopted boundary conditions matched the test conditions – the top of the specimens were free to both rotate and shorten longitudinally, whereas the bottom was only allowed to rotate. The movement of specimen ends was fixed to that of an eccentric reference point, positioned at the rotation point of both knife edges. The load was applied through the top reference point. The reference points were longitudinally offset by 50 mm, to model the distance between the knife edge rotation point and the specimen end (comprising 40 mm thick knife edges plus 10

mm thick end plates), and had an eccentricity e_0 to the centroid of the specimens equal to the calculated eccentricity from the tests.

The FE models included local and global geometric imperfections that took the form of the lowest local and global buckling mode shapes from a prior elastic buckling analysis. The imperfection amplitudes adopted were the measured value ω_0 and a fraction of the effective length $L/1000$ for the global imperfections and $t/10$ and $t/100$ for the local imperfections, with t being the section thickness of the specimen being modelled. The modified Riks method was used to enable the nonlinear post-ultimate response to be followed.

3.3. Validation

Finite element models of the twelve combined loading tests, at the member level from Section 2, were produced using the measured average geometric properties, with both the average tensile coupon properties and the compressive properties from the stub column tests. The numerical models were validated by comparing the normalised average predicted ultimate load $N_{\mathrm{u,FE}}/N_{\mathrm{u,exp}}$ and the mid-height lateral deformation at the ultimate load $\omega_{\mathrm{u,FE}}/\omega_{\mathrm{u,exp}}$ with the measured values, as shown in Tables 9 and 10 respectively. The mid-height lateral deformation at the ultimate load is less successfully replicated by the finite element models than the ultimate load. The ultimate load and mid-height deformation at the ultimate load are on average more closely predicted using the stub column material properties than the tensile coupon properties. The most accurate numerical predictions were on average attained with compressive material properties, a local imperfection amplitude of $t/10$ and a global imperfection amplitude of $L/1000$. The measured ultimate capacity $N_{\mathrm{u,exp}}$ is plotted against the predicted ultimate capacity $N_{\mathrm{u,FE}}$ (with a local imperfection amplitude of $t/10$ and a global imperfection amplitude of $L/1000$) in Figure 14, demonstrating that the numerical models can predict the ultimate load accurately. The measured mid-height lateral deformation at the ultimate test load $\omega_{\mathrm{u,exp}}$ is plotted against that at the predicted ultimate capacity $\omega_{\mathrm{u,FE}}$ (with the same local and global imperfection amplitude) in Figure 15. The mid-height lateral deflection is less accurately predicted than the ultimate capacity $N_{\mathrm{u,exp}}$ by the numerical models, with a number of the predictions lying close to or beyond the 10% error boundary plotted in Figure 15; this is attributed to the flat nature of the load-deformation curve in the region of the peak load; a small error in the peak load prediction results in a larger error in the corresponding predicted lateral deflection at the ultimate load.

The load-deformation relationships can also be compared, as shown in Figure 16 for the 80×1.5-1600-P, 80×1.5-1600-P-10E and 80×1.5-1600-P-30E specimens and in Figure 17 for the 101.6×1.5-1600-P-10E, 101.6×1.5-1600-P-40E and 101.6×1.5-1600-P-120E specimens; generally the numerical models can closely replicate the load-deformation history.

The developed models can therefore be considered to be able to reproduce the new experimental results, in particular the ultimate load, which can be used to evaluate the existing

Table 9: Summary of the average $N_{u,FE}/N_{u,exp}$ values for varying material properties and imperfection amplitudes

Material model	Tensile properties		Compressive properties		
Local imperfection amplitude	$t/10$	$t/10$	$t/10$	$t/10$	$t/100$
Global imperfection amplitude	L/1000	ω_0	L/1000	ω_0	ω_0
Mean $N_{u,FE}/N_{u,exp}$	1.107	1.120	1.029	1.042	1.042
COV $N_{u,FE}/N_{u,exp}$	0.042	0.036	0.032	0.027	0.027

Table 10: Summary of the average $\omega_{u,FE}/\omega_{u,exp}$ values for varying material properties and imperfection amplitudes

Material model	Tensile properties		Compressive properties		
Local imperfection amplitude	$t/10$	$t/10$	$t/10$	$t/10$	$t/100$
Global imperfection amplitude	L/1000	ω_0	L/1000	ω_0	ω_0
Mean $\omega_{u,FE}/\omega_{u,exp}$	0.797	0.780	0.983	0.976	0.977
COV $\omega_{u,FE}/\omega_{u,exp}$	0.140	0.140	0.151	0.129	0.130

EN 1993-1-4 (2015) beam-column design guidance.

3.4. Parametric study

Zhao et al. [27] undertook an extensive finite element study on stainless steel CHS under combined axial loading and bending moment at the cross-sectional level, and therefore in this parametric study only stainless steel CHS beam-column members were modelled. A Python script was written to allow a large number of finite element models to be produced and run without manual input. In total 25 cross-sections were modelled: six austenitic (A) cross-sections, nine duplex (D) cross-sections and ten ferritic (F) cross-sections, as reported in Table 11, using austenitic and duplex stainless steel material properties, respectively averaged from 106×3 and 88.9×2.6 CHS, reported in Buchanan et al. [15] and averaged 101.6×1.5 CHS ferritic stainless steel properties from this study for the adopted compressive material models. A local imperfection amplitude of $t/10$ and a global imperfection of $L/1000$ was used for all models. The outer diameter D, wall thickness t, EN 1993-1-4 (2015) cross-section class, minimum $\overline{\lambda}_{min}$ and maximum $\overline{\lambda}_{max}$ global slendernesses, minimum $e_{0,min}$ and maximum $e_{0,max}$ applied eccentricities and number of FE models per cross-section n are listed in Table 11. The local slendernesses were varied to model cross-section classes 1–3, the member lengths were chosen to provide a range of global slenderness values up to a maximum of $\overline{\lambda} = 2.6$ and the eccentricities varied from 0 mm to 805 mm to provide a range of axial load to bending moment ratios.

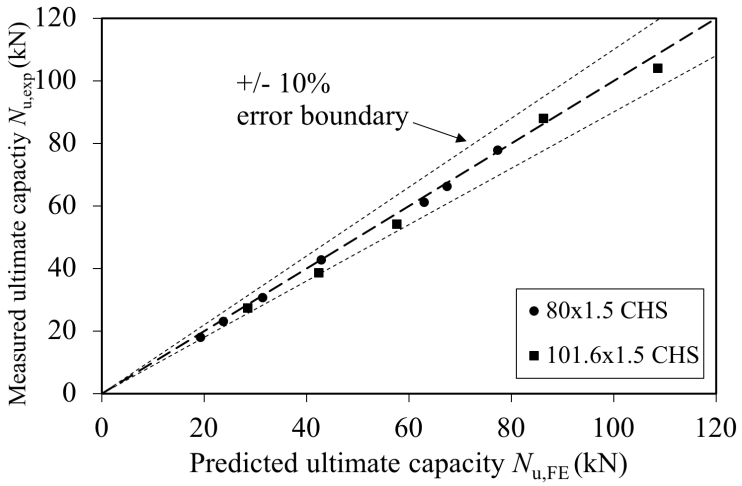

Figure 14: Deformed 80×1.5 CHS long beam-columns, with load eccentricity increasing from bottom to top.

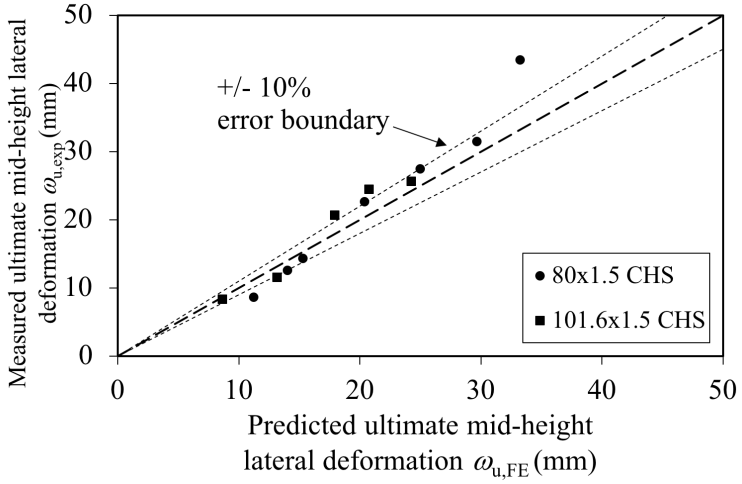

Figure 15: Deformed 101.6×1.5 CHS long beam-columns, with load eccentricity increasing from bottom to top.

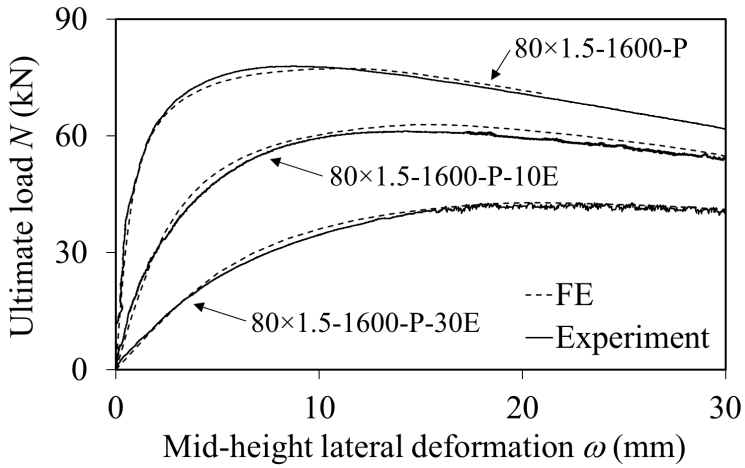

Figure 16: Experimental and FE load mid-height lateral deformation curves for the 80×1.5-1600-P, 80×1.5-1600-P-10E and 80×1.5-1600-P-30E specimens.

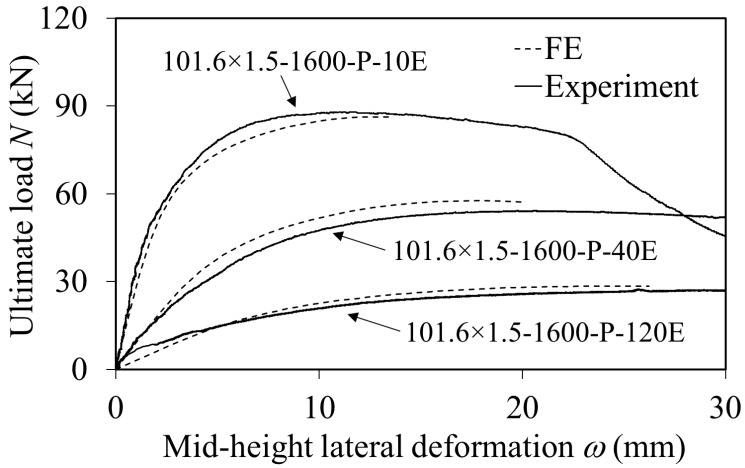

Figure 17: Experimental and FE load mid-height lateral deformation curves for the 101.6×1.5-1600-P-10E, 101.6×1.5-1600-P-40E and 101.6×1.5-1600-P-120E specimens.

Table 11: Summary of the eccentricity loaded pin-ended parametric study specimens.

Section	Grade	Type	D (mm)	t (mm)	D/t	$D/(t\varepsilon^2)$	EN 1993-1-4 (2015) compressive class	Local slenderness $\overline{\lambda}_c$	Global slenderness $\overline{\lambda}_{min}$	Global slenderness $\overline{\lambda}_{max}$	Eccentricity (mm) $e_{0,min}$	Eccentricity (mm) $e_{0,max}$	Number of FE models
100×8	1.4432	A	100	8.0	12.5	17.8	1	0.13	0.39	1.83	0	450	81
100×6	1.4432	A	100	6.0	16.7	23.7	1	0.15	0.25	2.59	7	750	96
100×5	1.4432	A	100	5.0	20.0	28.4	1	0.16	0.42	1.51	0	190	68
100×4	1.4432	A	100	4.0	25.0	35.5	1	0.18	0.56	2.05	0	550	94
100×3	1.4432	A	100	3.0	33.3	47.4	1	0.21	0.26	2.59	7	750	140
100×2	1.4432	A	100	2.0	50.0	71.0	3	0.26	0.44	1.90	0	350	115
100×11	1.4462	D	100	11.0	9.1	25.4	1	0.15	0.43	2.59	10	780	94
100×9	1.4462	D	100	9.0	11.1	31.0	1	0.17	0.83	1.93	0	420	53
100×8	1.4462	D	100	8.0	12.5	34.9	1	0.18	0.65	1.69	5	400	55
100×7	1.4462	D	100	7.0	14.3	39.9	1	0.19	0.54	1.62	0	500	56
100×5.5	1.4462	D	100	5.5	18.2	50.8	2	0.22	0.43	1.49	0	500	94
100×5	1.4462	D	100	5.0	20.0	55.9	2	0.23	0.63	1.06	5	140	22
100×4.5	1.4462	D	100	4.5	22.2	62.1	2	0.24	0.89	2.37	1	320	80
100×4	1.4462	D	100	4.0	25.0	69.8	2	0.25	0.42	0.94	0	420	35
100×3.5	1.4462	D	100	3.5	28.6	79.8	3	0.27	0.43	2.59	0	805	132
100×8	1.4512	F	100	8.0	12.5	20.3	1	0.14	0.58	2.04	0	260	55
100×6	1.4512	F	100	6.0	16.7	27.1	1	0.16	0.24	2.59	9	760	116
100×5	1.4512	F	100	5.0	20.0	32.5	1	0.17	0.52	1.78	0	500	95
100×4	1.4512	F	100	4.0	25.0	40.7	1	0.19	0.32	1.48	0	550	97
100×3.5	1.4512	F	100	3.5	28.6	46.5	1	0.21	1.69	1.98	380	590	16
100×3	1.4512	F	100	3.0	33.3	54.2	2	0.22	0.40	1.58	0	550	75
100×2.6	1.4512	F	100	2.6	38.5	62.6	2	0.24	0.71	1.18	2	320	39
100×2.3	1.4512	F	100	2.3	43.5	70.7	3	0.26	0.30	1.41	0	320	70
100×2.2	1.4512	F	100	2.2	45.5	73.9	3	0.26	0.28	1.41	0	230	108
100×2	1.4512	F	100	2.0	50.0	81.3	3	0.27	0.24	2.59	9	720	130

4. Existing and proposed design provisions

EN 1993-1-4 (2015) includes guidance for the design of both cross-sections and members under combined axial loading and bending moment for stainless steel CHS elements. The continuous strength method (CSM) has also been developed for stainless steel CHS cross-sections under combined axial loading and bending moment. The suitability of the current and proposed design guidance is assessed in this section using the experimental results at the cross-section level and the new and existing member level test results and numerical models at the member level. The measured geometric and compressive material properties are used in the comparisons and all safety factors are taken to be equal to unity.

4.1. EN 1993-1-4 (2015) cross-section design provisions

The current EN 1993-1-4 (2015) guidance for the design of CHS under combined axial loading and bending moment follows the same approach as for structural carbon steel in EN 1993-1-1 (2014). A nonlinear interaction curve is utilised for the combined loading resistance of class 1 and 2 cross-sections,

$$M_{\mathrm{Ed}} \leq M_{\mathrm{N,Rd}} = M_{\mathrm{pl,Rd}} \left(1 - n^{1.7}\right) \tag{9}$$

where M_{Ed} is the design ultimate bending moment determined from Equation 6, $M_{\mathrm{N,Rd}}$ is the design plastic moment resistance reduced due to the applied axial force N_{Ed}, $M_{\mathrm{pl,Rd}}$ is the plastic moment capacity (the product of the plastic section modulus W_{pl} and $\sigma_{0.2}$) and $n = N_{\mathrm{Ed}}/N_{\mathrm{pl,Rd}}$ is the axial load level, with N_{Ed} being the design ultimate axial load and $N_{\mathrm{pl,Rd}}$ being the design plastic resistance of the gross cross-section (the product of the gross cross-sectional area A and the 0.2% proof stress $\sigma_{0.2}$). For class 3 and 4 cross-sections the design expression is a linear summation of the separate axial and bending utilisation ratios with a limit of unity,

$$\frac{N_{\mathrm{Ed}}}{N_{\mathrm{Rd}}} + \frac{M_{\mathrm{Ed}}}{M_{\mathrm{Rd}}} \leq 1 \tag{10}$$

where N_{Rd} is the pure compression design resistance and M_{Rd} is the pure bending design resistance. For class 3 cross-sections, N_{Rd} is the product of the gross cross-sectional area A and the 0.2% proof stress $\sigma_{0.2}$, while for class 4 cross-sections, the effective cross-sectional area A_{eff} is utilised. For class 3 cross-sections M_{Rd} is the elastic moment capacity M_{el} (the product of the elastic section modulus W_{el} and $\sigma_{0.2}$) while for slender class 4 cross-sections the design capacity is the product of the effective section modulus W_{eff} and $\sigma_{0.2}$. The effective area A_{eff} and effective section modulus W_{eff} can be determined using the slender cross-section design formulae proposed in [22, 44], which are adaptations of the BS 5950-1 (2000) expressions, updated according to the EN 1993-1-4 (2015) class 3 slenderness limits, as reproduced previously for A_{eff} in Equation 3. The experimental results normalised by their full cross-sectional capacities are shown in Figures 18 and 19 along with the EN 1993-1-4 (2015) linear interaction curve.

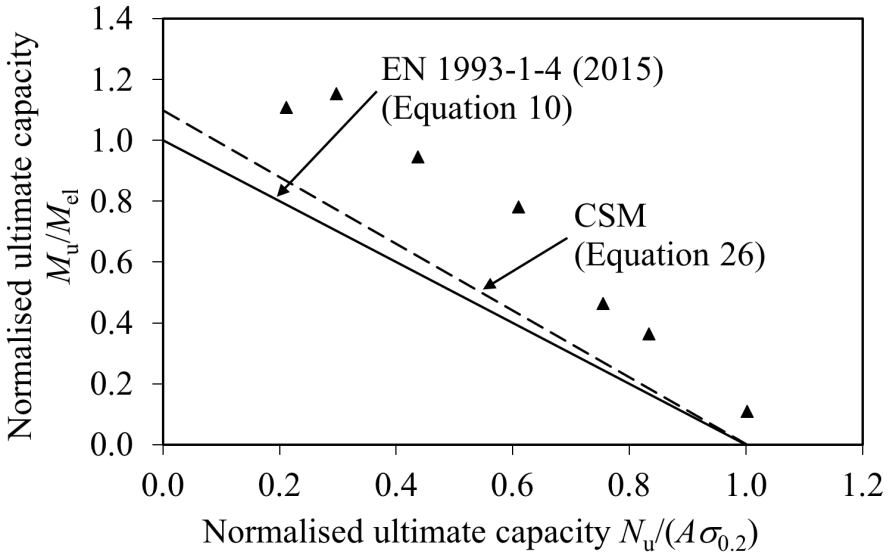

Figure 18: Comparison between 80×1.5 CHS cross-section test results under combined loading with interaction curves.

EN 1993-1-4 (2015) does not currently have guidance for cross-section classification of CHS under combined loading. Linear interpolation between the compressive and bending class 3 slenderness limits was therefore used to define the class 3 slenderness limit under combined loading as,

$$\frac{D}{t\varepsilon^2} = 185 - 95\psi \tag{11}$$

with ψ being the ratio of the difference and sum of the compressive σ_c and bending σ_b stresses at the ultimate load,

$$\psi = \frac{\sigma_c - \sigma_b}{\sigma_c + \sigma_b}, \tag{12}$$

which is similar to the approach used for EHS by Gardner et al. [57]. The 80×1.5 and 101.6×1.5 CHS cross-sections are both class 3 under combined loading for the ratios of axial load to bending moment employed in the eccentrically loaded tests performed in this study.

Figures 18 and 19 show that the current Eurocode 3 design guidance offers safe side predictions for class 3 ferritic stainless steel CHS under combined axial loading and bending moment, although it is rather conservative, indicating that additional structural efficiency may be sought.

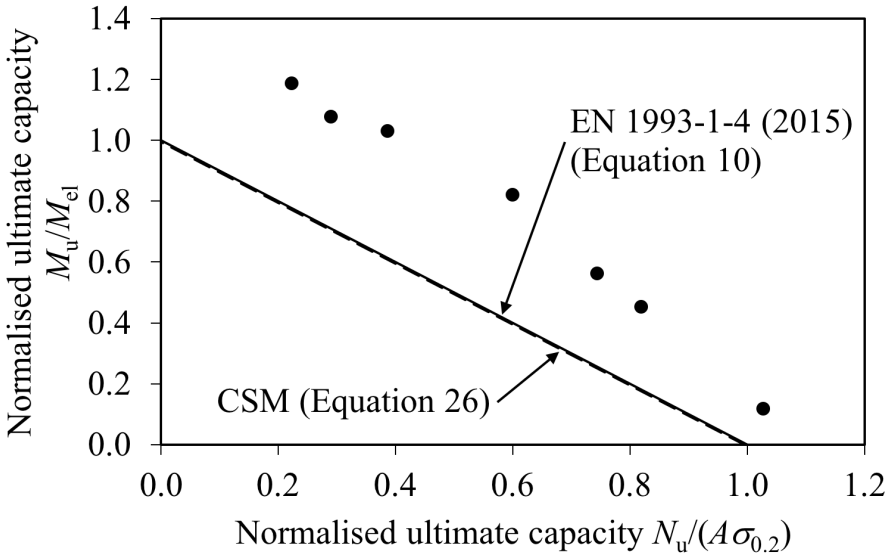

Figure 19: Comparison between 101.6×1.5 CHS cross-section test results under combined loading with interaction curves.

4.2. The continuous strength method design provisions

The continuous strength method (CSM) has been developed to provide a more rational approach to the design of metallic structures. Cross-section classification is replaced with a continuous relationship between cross-section slenderness and deformation capacity, called the base curve, reflecting the continuous nature of the variation of cross-section capacity with local slenderness. A strain hardening material model is also adopted, representing the observed behaviour in material tests, with an increase in strength above the yield strength with increasing plastic deformation. The CSM was extended to cover non-slender and slender structural carbon steel, stainless steel and aluminium CHS in pure compression and bending by Buchanan et al. [22] and for non-slender stainless steel CHS under combined axial loading and bending moment by Zhao et al. [27]. Zhao et al. [27] adopted the CSM cross-sectional compression and bending resistances as the end points of the linear interaction curve. The CSM axial resistance N_{csm} can be determined from Equations 13 and 14 for non-slender and slender cross-sections respectively, and the bending resistance M_{csm} can be obtained from Equations 15 and 16 for non-slender and slender cross-sections respectively.

$$N_{csm} = A\sigma_{csm} \text{ for } \overline{\lambda}_c \leq 0.3 \tag{13}$$

$$N_{csm} = \frac{\varepsilon_{csm}}{\varepsilon_y} A\sigma_{0.2} \text{ for } 0.3 < \overline{\lambda}_c \leq 0.6 \tag{14}$$

$$M_{csm} = M_{pl}\left[1 + \frac{E_{sh}}{E}\frac{W_{el}}{W_{pl}}\left(\frac{\varepsilon_{csm}}{\varepsilon_y} - 1\right) - \left(1 - \frac{W_{el}}{W_{pl}}\right) / \left(\frac{\varepsilon_{csm}}{\varepsilon_y}\right)^2\right] \text{ for } \overline{\lambda}_c \leq 0.3 \tag{15}$$

$$M_{csm} = \frac{\varepsilon_{csm}}{\varepsilon_y} W_{el} \sigma_{0.2} \text{ for } 0.3 < \overline{\lambda}_c \leq 0.6 \tag{16}$$

The local slenderness $\overline{\lambda}_c$ can be calculated from Equation 17, with the elastic critical buckling stress σ_{cr} determined from Equation 18 where ν is the Poisson's ratio.

$$\overline{\lambda}_c = \sqrt{\frac{\sigma_{0.2}}{\sigma_{cr}}} \tag{17}$$

$$\sigma_{cr} = \frac{E}{\sqrt{3(1-\nu^2)}} \frac{2t}{D} \tag{18}$$

The allowable deformation capacity, also known as the strain ratio $\varepsilon_{csm}/\varepsilon_y$, of the cross-section can then be determined from the base curves for non-slender and slender circular cross-sections, given by Equations 19 and 20 respectively with $C_1 = 0.10$ for austenitic and duplex stainless steel and $C_1 = 0.40$ for ferritic grades,

$$\frac{\varepsilon_{csm}}{\varepsilon_y} = \frac{4.44 \times 10^{-3}}{\overline{\lambda}_c{}^{4.5}} \text{ for } \overline{\lambda}_c \leq 0.3 \text{ but } \frac{\varepsilon_{csm}}{\varepsilon_y} \leq \min\left(\Omega, \frac{C_1 \varepsilon_u}{\varepsilon_y}\right) \tag{19}$$

$$\frac{\varepsilon_{csm}}{\varepsilon_y} = \left(1 - \frac{0.224}{\overline{\lambda}_c{}^{0.342}}\right) \frac{1}{\overline{\lambda}_c{}^{0.342}} \text{ for } 0.3 < \overline{\lambda}_c \leq 0.6, \tag{20}$$

depending upon whether the local slenderness $\overline{\lambda}_c$ of the cross-section is below or above the yield slenderness limit ($\overline{\lambda}_c = 0.3$). Below this limit, benefit can be derived from strain hardening. The parameter Ω defines the maximum strain ratio that can be tolerated at ultimate limit state for a given project, with a recommended value of 15.

The CSM limiting material stress σ_{csm} can be calculated from Equations 21 and 22,

$$\sigma_{csm} = E \varepsilon_{csm} \text{ for } \frac{\varepsilon_{csm}}{\varepsilon_y} < 1 \tag{21}$$

$$\sigma_{csm} = \sigma_{0.2} + E_{sh} \varepsilon_y \left(\frac{\varepsilon_{csm}}{\varepsilon_y} - 1\right) \text{ for } \frac{\varepsilon_{csm}}{\varepsilon_y} \geq 1, \tag{22}$$

depending upon whether the strain ratio $\varepsilon_{csm}/\varepsilon_y$ is less than or greater than unity, where E_{sh} is the strain hardening modulus, from Equation 23, and ε_y is the yield strain ($\sigma_{0.2}/E$). The material strain ε_u corresponding to the ultimate tensile stress σ_u can be calculated from Equation 24. The C_2 and C_3 coefficients are defined in Table 12 [58, 59].

$$E_{\text{sh}} = \frac{\sigma_{\text{u}} - \sigma_{0.2}}{C_2 \varepsilon_{\text{u}} - \varepsilon_{\text{y}}} \tag{23}$$

$$\varepsilon_{\text{u}} = C_3 \left(1 - \frac{\sigma_{0.2}}{\sigma_{\text{u}}}\right) \tag{24}$$

Table 12: Summary of coefficients for the CSM material model.

Type of stainless steel	C_1	C_2	C_3
Austenitic	0.10	0.16	1.00
Duplex	0.10	0.16	1.00
Ferritic	0.40	0.45	0.60

A nonlinear interaction curve based on the theoretical fully plastic interaction relationship for CHS under combined axial compression and bending moment (adopted by EN 1993-1-4 (2015) and reproduced here as Equation 9) from Rondal et al. [60] was also proposed by Zhao et al. [27] below a local slenderness transition point of $\overline{\lambda}_c = 0.27$, reverting to the linear interaction curve for compatibility with the elastic end points as the slenderness approaches the yield slenderness limit of $\overline{\lambda}_c = 0.3$. The nonlinear and linear interaction curves are reproduced as

$$M_{Ed} \leq M_{R,csm} = 1.04 M_{csm} \left(1 - {n_{csm}}^{1.7}\right) \leq M_{csm} \text{ for } \overline{\lambda}_c \leq 0.27 \tag{25}$$

and

$$\frac{N_{Ed}}{N_{csm}} + \frac{M_{Ed}}{M_{csm}} \leq 1 \text{ for } \overline{\lambda}_c > 0.27 \tag{26}$$

respectively, where $n_{csm} = N_{Ed}/N_{csm}$.

The 80×1.5 CHS cross-section has a local slenderness of $\overline{\lambda}_c = 0.28$ and thus Equations 13 and 15 are employed to determine the CSM axial and bending resistances, respectively, while Equation 26 is used to define the interaction. The 101.6×1.5 CHS cross-section has a local slenderness of $\overline{\lambda}_c = 0.31$ and the slender CSM axial and bending resistances, Equations 14 and 16 respectively, have been applied as the interaction curve end points in Equation 26. The CSM interaction curves are plotted in Figures 18 and 19 along with the experimental data and can be seen to offer improved predictions of the cross-sectional capacities under combined loading for the 80×1.5 CHS cross-section. The application of the CSM compressive and bending end points to the 101.6×1.5 CHS cross-section yields very similar results to EN 1993-1-4 (2015), since the cross-section is only marginally beyond the yield slenderness limit.

4.3. EN 1993-1-4 (2015) member design provisions

The current EN 1993-1-4 (2015) design approach for stainless steel beam-columns utilises the same form of interaction formulae as provided for structural carbon steel in EN 1993-1-1 (2014), although the interaction factors have been modified to account for the influence of the nonlinear material response on member instability. The beam-column combined loading design expression is reproduced as follows,

$$\frac{N_{Ed}}{N_{b,Rd}} + k \left(\frac{M_{Ed} + N_{Ed} e_N}{\beta_w W_{pl} \sigma_{0.2}} \right) \leq 1 \tag{27}$$

where N_{Ed} is the design ultimate axial load, M_{Ed} is the design first order bending moment (being N_{Ed} multiplied by $(e_0 + \omega_0)$, which is different to that used at the cross-section level (Equation 6), k is an interaction factor that captures the amplification of moments due to second order effects (i.e. lateral deflections), $N_{\mathrm{b,Rd}}$ is the flexural buckling design resistance, e_{N} is the shift in the neutral axis (for local buckling of slender cross-sections) when the cross-section is subjected to uniform compression (which is zero for doubly symmetric cross-sections), and β_{w} is a factor which modifies the expression for the various cross-section classes — for class 1 and 2 cross-sections $\beta_{\mathrm{w}} = 1.0$, for class 3 cross-sections $\beta_{\mathrm{w}} = W_{\mathrm{el}}/W_{\mathrm{pl}}$ and for class 4 cross-sections $\beta_{\mathrm{w}} = W_{\mathrm{eff}}/W_{\mathrm{pl}}$. The EN 1993-1-4 (2015) interaction factor k can be calculated using

$$1.2 \leq k = 1 + 2\left(\overline{\lambda} - 0.5\right)\frac{N_{\mathrm{Ed}}}{N_{\mathrm{b,Rd}}} \leq 1.2 + 2\frac{N_{\mathrm{Ed}}}{N_{\mathrm{b,Rd}}}. \tag{28}$$

The experimental results normalised by their cross-sectional capacities are shown in Figures 20 and 21 along with the EN 1993-1-4 (2015) member level interaction curves; the point at which the interaction curves meet the horizontal axis corresponds to the buckling reduction factor χ. Classification under combined loading was again undertaken using Equations 11 and 12, and both the 80×1.5 and 101.6×1.5 CHS cross-sections were found to be class 3 for the ratios of axial load to bending moment employed in the eccentrically loaded tests; the concentrically loaded 101.6×1.5-1600-P CHS specimen was classified as class 4 and therefore the effective cross-sectional area A_{eff} and section modulus W_{eff} were used. Figures 20 and 21 show that the current guidance is conservative towards the bending end point, which mirrors the findings of Zhao et al. [27] and is attributed to the neglecting of strain hardening for the bending end point and to conservative interaction factors, but the test points lie on the unsafe side towards the compression end point.

4.4. Proposed member design provisions

Improvements to the current EN 1993-1-4 (2015) design approach for stainless steel beam-columns are proposed herein and focus on two key areas: the interaction factor and the two end points.

4.4.1. Improved end points

The current pure compression end point is the flexural buckling resistance $N_{\mathrm{b,Rd}}$, which has been previously observed to provide unconservative predictions for certain global slenderness values [9, 15, 24, 25, 61–64]. Buchanan et al. [15] proposed a new flexural buckling curve that is compatible with the existing design approach in EN 1993-1-4 (2015), with $N_{\mathrm{b,Rd}}$ determined from Equation 29,

$$N_{\mathrm{b,Rd}} = \frac{\chi A \sigma_{0.2}}{\gamma_{\mathrm{M1}}} \text{ for class 1-3 cross-sections} \tag{29}$$

where the reduction factor χ is determined from Equation 30, A is the cross-sectional area (A_{eff} for class 4 cross-sections) and γ_{M1} is the partial safety factor. The operational

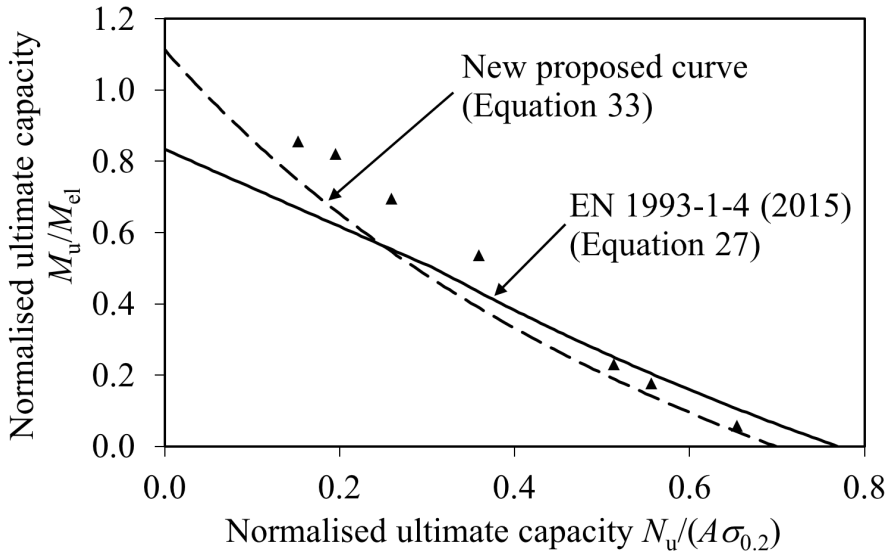

Figure 20: Comparison of 80×1.5 CHS beam-column member test results with interaction curves.

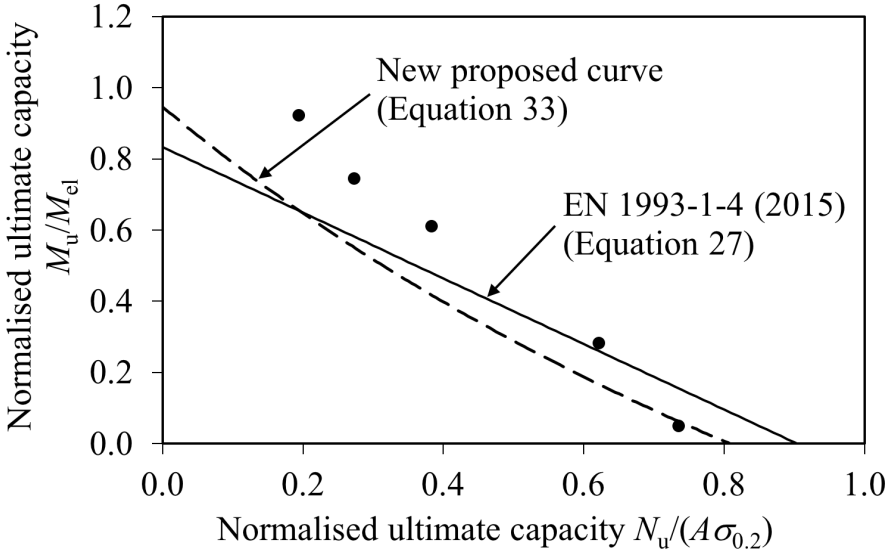

Figure 21: Comparison of 101.6×1.5 CHS beam-column member test results with interaction curves.

parameter ϕ is calculated using Equation 31, with the imperfection parameter η determined from Equation 32, in which the imperfection factor $\alpha = 0.49$ and recalibrated [15] limiting slenderness $\overline{\lambda}_0 = 0.20$. The imperfection factor α accommodates the effects of initial eccentricities, geometric imperfections and residual stresses. The same approach is proposed in the present paper, with $\alpha = 0.49$ corresponding to an out-of-straightness of approximately $L/200$.

$$\chi = \frac{1}{\phi + \sqrt{\phi^2 - \overline{\lambda}^2}} \tag{30}$$

$$\phi = \frac{1}{2}\left(1 + \eta + \overline{\lambda}^2\right) \tag{31}$$

$$\eta = \alpha\left(\overline{\lambda} - \overline{\lambda}_0\right) \tag{32}$$

The CSM bending resistance M_{csm}, which has been observed to provide more accurate predictions of the bending capacity of CHS [22], can be utilised as the pure bending end point. The CSM bending resistances were previously provided as Equations 15 and 16 for non-slender and slender cross-sections.

These proposals can be used to provide more suitable end points; the new flexural buckling curve can be used to predict a more appropriate flexural buckling resistance $N_{\mathrm{b,Rd}}$, while the CSM bending resistance M_{csm} allows for greater bending capacities to be attained through the base curve and material strain hardening. An advantage of improved end points is that the interaction factor does not need to compensate for their inaccuracies and is therefore more representative of the observed physical behaviour.

4.4.2. Improved interaction factor

The new proposed beam-column design expression is as follows,

$$\frac{N_{\mathrm{Ed}}}{N_{\mathrm{b,Rd}}} + k_{\mathrm{csm}}\frac{M_{\mathrm{Ed}}}{M_{\mathrm{csm,Rd}}} \leq 1 \tag{33}$$

where k_{csm} is the new interaction factor, which is determined using the same procedure as Greiner and Lindner [65], Boissonnade et al. [66] and Zhao et al. [35]. Individual k_{csm} factors are calculated for the experimental and numerical dataset using

$$k_{\mathrm{csm}} = \left(1 - \frac{N_{\mathrm{Ed}}}{N_{\mathrm{b,Rd}}}\right)\frac{M_{\mathrm{csm,Rd}}}{M_{\mathrm{Ed}}}, \tag{34}$$

which is a rearrangement of Equation 33. Simplified formulae can then be fitted to the data for different axial compressive load levels $n = N_{\mathrm{Ed}}/N_{\mathrm{b,Rd}}$.

Data for seven compressive load levels with $n = 0.2$ to $n = 0.8$, in steps of 0.1, were isolated from the full dataset and the k_{csm} interaction factor values plotted with varying global

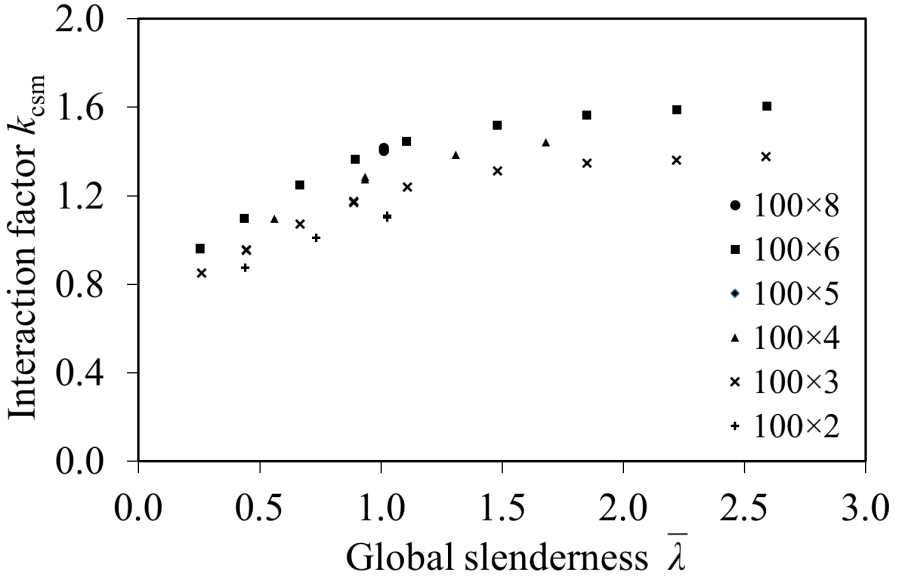

Figure 22: k_{csm} factors determined from the numerical dataset for the austenitic stainless steel specimens with a load level of $n = 0.2$.

Table 13: Proposed stainless steel CHS interaction curve coefficients.

Type	D_1	D_2	D_3
Austenitic	2.5	0.30	1.3
Duplex	2.0	0.38	1.3
Ferritic	1.9	0.35	1.3

slenderness $\overline{\lambda}$, as shown in Figure 22 for the austenitic stainless steel dataset with $n = 0.2$. The simplified design expression for k_{csm} is taken as the typical two-stage linear piecewise form [35, 65, 66],

$$k_{\text{csm}} = 1 + D_1 \left(\overline{\lambda} - D_2\right) n \leq 1 + D_1 \left(D_3 - D_2\right) n \tag{35}$$

where D_1 and D_2 are coefficients defining the linear relationship between the interaction factor k_{csm} and the global slenderness $\overline{\lambda}$ in the $\overline{\lambda} \leq D_3$ low slenderness range, beyond which k_{csm} has a constant value of $(1 + D_1 \left(D_3 - D_2\right) n)$. The D_1 and D_2 coefficients for the discrete compressive load levels were calculated from a regression fit between the upper bound of the assembled dataset and Equation 35 for $0.2 \leq \overline{\lambda} \leq 1.2$; the final D_1 and D_2 coefficients are averaged values for all of the compressive load levels and are listed in Table 13 for the three types of stainless steel used in construction. The D_1 and D_2 coefficients have been adjusted slightly such that their product, across the three types of stainless steel, is roughly equal, resulting in a consistent value when the global slenderness $\overline{\lambda}$ tends to zero. The D_3 coefficients are determined by fitting Equation 35 to the upper bound of the dataset for $n \leq 0.4$, and are also provided in Table 13.

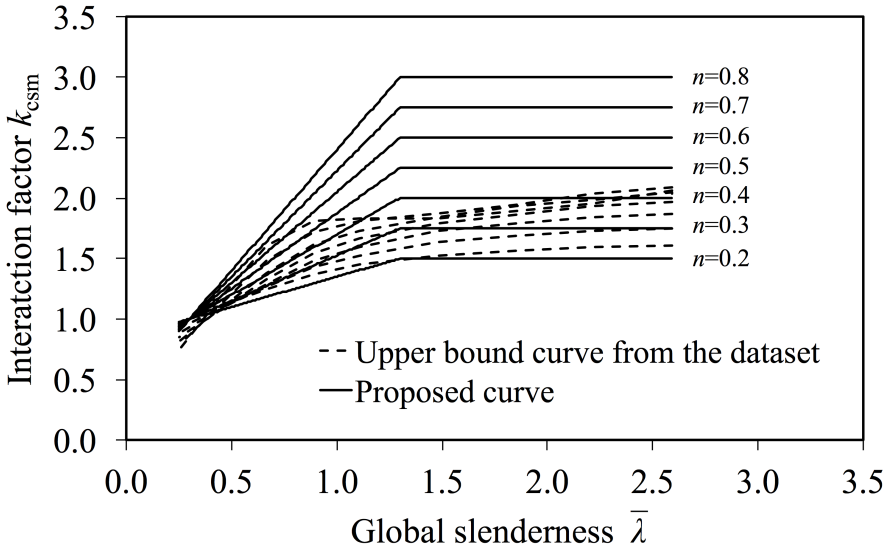

Figure 23: Proposed and FE-calculated interaction factors k_{csm} for the austenitic stainless steel beam-column CHS specimens.

The FE-calculated and proposed interaction factors k_{csm} are plotted for the austenitic stainless steel dataset in Figure 23, with a dashed line passing through the upper bound of the calculated k_{csm} values for the various axial load levels n. It is clear from Figure 23 that there is a large difference between the proposed interaction factors and the calculated values for the assembled dataset at high axial compressive load levels n and at high $\overline{\lambda}$ global slenderness values; however, for members with high slendernesses and high axial load levels, the structural response is controlled by column buckling, rather than bending resistance, and therefore this disparity is acceptable and in line with previous developments [35, 65, 67], and the resulting errors for beam-column design are small.

When the global slenderness tends to zero the new proposed beam-column expression becomes

$$\frac{N_{\mathrm{Ed}}}{N_{\mathrm{pl,Rd}}} + \left(1 - 0.75\frac{N_{\mathrm{Ed}}}{N_{\mathrm{pl,Rd}}}\right)\frac{M_{\mathrm{Ed}}}{M_{\mathrm{csm,Rd}}} \leq 1 \tag{36}$$

for austenitic stainless steel, where $N_{\mathrm{pl,Rd}}$ is the yield load. This expression is similar to the CSM cross-section interaction curve presented previously as Equation 25, as shown in Figure 24 for a cross-section on the class 3 limit.

The new proposed interaction factor k_{csm} and end points are plotted in Figures 20 and 21. The benefit from utilising the increased CSM bending resistance M_{csm} and the more appropriate pure compression end point is apparent; the experimental results are now closer to and typically above the proposed interaction curve.

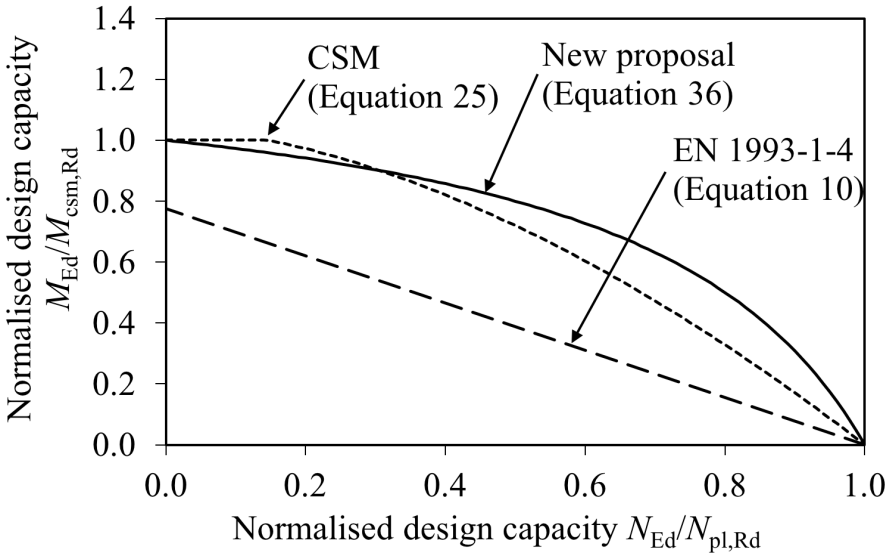

Figure 24: Comparison of the interaction curves at the cross-section level.

4.5. Discussion of the existing and new design provisions

The existing and proposed design approaches for stainless steel CHS elements under combined loading at the local and global level are appraised using the assembled experimental and numerical dataset in this sub-section. The predicted capacity from the various design methods can be calculated assuming proportional loading, as defined in Figure 25.

At the cross-section level, the average ultimate compressive capacity in the presence of the co-existent bending normalised by the Eurocode and CSM design capacities, $N_u/N_{u,EC3}$ and $N_u/N_{u,csm}$ respectively, is provided in Table 14. The 80×1.5-350-P-100E CHS result is omitted from the results in Table 14, due to the end plates yielding in bending. The EN 1993-1-4 (2015) and CSM interaction curves are plotted with the experimental data in Figures 18 and 19. The current Eurocode 3 design guidance offers rather conservative predictions of the combined axial loading and bending moment capacity, while the CSM offers on average more accurate and less scattered resistance predictions, reflected by a mean test-to-predicted capacity ratio closer to unity and lower coefficient of variation (COV) values. The 101.6×1.5 CHS cross-section resistance is slightly more accurately predicted by the existing EN 1993-1-4 (2015) approach due to the cross-section being classified as class 3 under combined loading, whereas for the CSM it is classified as a slender cross-section and is therefore predicted to attain a slightly lower resistance. The overall improvements in resistance predictions under combined axial loading and bending moment obtained using the CSM can also apply to other metallic materials.

At the member level, the average ultimate compressive capacity in the presence of the co-existent bending normalised by the Eurocode and new proposed resistance predictions,

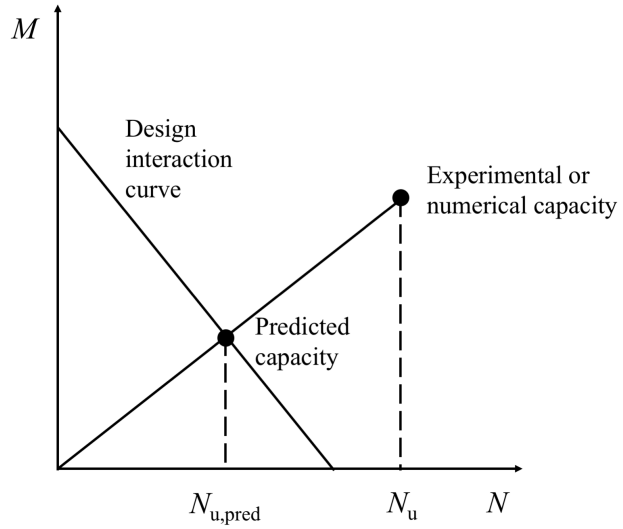

Figure 25: Definition of $N_{u,pred}$ on the moment-axial interaction curve.

Table 14: Comparison of the ultimate and predicted combined axial load and bending strength.

Cross-section	Mean		COV	
	$N_u/N_{u,EC3}$	$N_u/N_{u,csm}$	$N_u/N_{u,EC3}$	$N_u/N_{u,csm}$
80×1.5	1.29	1.22	0.10	0.07
101.6×1.5	1.33	1.34	0.08	0.08
All test specimens	1.31	1.28	0.09	0.09

Table 15: Comparison of the experimental ultimate and predicted beam-column strengths considering both new and existing test results.

Cross-section	Source	Type	Mean		COV	
			$N_u/N_{u,EC3}$	$N_u/N_{u,proposed}$	$N_u/N_{u,EC3}$	$N_u/N_{u,proposed}$
140×2	Talja [7]	A	1.14	1.27	0.03	0.01
140×4	Talja [7]	A	1.12	1.24	0.07	0.03
60.5×2.8	Zhao et al. [23]	A	1.00	1.07	0.02	0.02
76.3×3	Zhao et al. [23]	A	0.97	1.03	0.04	0.02
80×1.5	This study	F	1.09	1.10	0.12	0.05
101.6×1.5	This study	F	1.13	1.19	0.13	0.07
Average	-	-	1.06	1.13	0.10	0.08

$N_u/N_{u,EC3}$ and $N_u/N_{u,proposed}$, are provided in Table 15 for the new and existing CHS experimental results, including the austenitic stainless steel beam-column results from Talja [7] and Zhao et al. [23], and in Table 16 for the full experimental and numerical dataset. The EN 1993-1-4 (2015) and new proposed interaction curves are plotted with the ferritic stainless steel CHS experimental beam-column data in Figures 20 and 21. The experimental only dataset from Table 15 shows that the new proposed end points and interaction factor result in less scattered, but also slightly less accurate predictions, than the existing EN 1993-1-4 (2015) approach, although the average $N_u/N_{u,proposed}$ values for all of the individual cross-sections are greater than unity (i.e. safe-sided predictions) with the new proposals. The apparent reduced accuracy is attributed to the more conservative compressive end point, though it can be seen from Figures 20 and 21 that towards the pure compression end, the existing interaction curve results in a number of predictions on the unsafe side, which artificially reduces the average normalised ultimate load. The new proposal for stainless steel CHS beam-columns can be seen to be more accurate (by approximately 4% on average) and consistent (with a dramatically lower COV) in its resistance predictions than the current EN 1993-1-4 (2015) approach for the full experimental and numerical dataset in Table 16. The reduced COV is particularly beneficial in the reliability analysis in Section 5. The shortcomings of the pure compression end point of the existing EN 1993-1-4 (2015) interaction curve applies particularly to stainless steel CHS, as demonstrated by the proposed recalibration of the limiting slenderness $\overline{\lambda}_0$ [15]. The overly conservative pure bending end point of the existing EN 1993-1-4 (2015) interaction curve will also apply to CHS of other steel types, and the proposed CSM bending resistance M_{csm} provides a more accurate prediction of the bending resistance.

A further comparison can be made between the existing EN 1993-1-4 (2015) approach and the new proposal by plotting the ultimate compressive capacity in the presence of the co-existent bending moment normalised by the predicted value against the angle parameter θ, as shown

Table 16: Comparison between test or FE ultimate strength and predicted ultimate strength for the full experimental and numerical beam-column dataset.

Type	Mean		COV	
	$N_u/N_{u,EC3}$	$N_u/N_{u,proposed}$	$N_u/N_{u,EC3}$	$N_u/N_{u,proposed}$
Austenitic	1.12	1.10	0.10	0.06
Duplex	1.18	1.12	0.09	0.05
Ferritic	1.17	1.10	0.12	0.05
Average	1.15	1.11	0.11	0.05

in Figures 27 to 32. The angle parameter θ is defined as

$$\theta = \tan^{-1}\left(\frac{N_{Ed}/N_R}{M_{Ed}/M_R}\right), \tag{37}$$

where N_R and M_R are the predicted pure compression and bending member strengths, with $\theta = 0°$ corresponding to pure bending and $\theta = 90°$ being pure compression, as shown in Figure 26. It is again apparent that the new proposal provides more accurate beam-column resistance predictions than the current EN 1993-1-4 (2015) method. Note that the proposed interaction factors k_{csm} (defined by the corresponding values for D_1, D_2 and D_3 given in Table 13) may also be conservatively employed with the traditional EN 1993-1-4 (2015) end points, with the column buckling curve appropriately updated (i.e. $\alpha = 0.49$ and $\overline{\lambda}_0 = 0.20$). The adoption of end points and an interaction curve is commonplace in design standards [68, 69] and the proposed changes in this section could also be applied to other international design standards.

5. Reliability analyses

In the European design standards, member level resistances are divided by a partial factor γ_{M1}, as seen in Equation 29, to ensure that structures are designed with an appropriate level of reliability. The partial factors are determined using a procedure outlined in Annex D of EN 1990 (2005). The experimental and numerical dataset has been used to reassess the γ_{M1} partial factor for the current EN 1993-1-4 (2015) CHS beam-column design approach and the new proposed design approach, as reported in Tables 17 and 18 respectively, where n is the size of the dataset, the over-strength factor is the mean yield strength normalised by the nominal yield strength, V_{f_y} is the coefficient of variation of the yield strength, $V_{geometry}$ is the coefficient of variation of the geometry of the cross-section, $k_{d,n}$ is the fractile factor and is related to the size of the dataset, b is the average ratio of the experimental or numerical resistance to the model resistance and V_δ is the coefficient of variation of the tests relative to the resistance model. The over-strength factor and the coefficients of variation of the yield strength and geometry V_{f_y} and $V_{geometry}$ used in the statistical analysis were taken from Afshan et al. [70]. The least squares approach from Annex D of EN 1990 (2005) was not used for the calculation of the b parameter as this is deemed to bias the value towards the

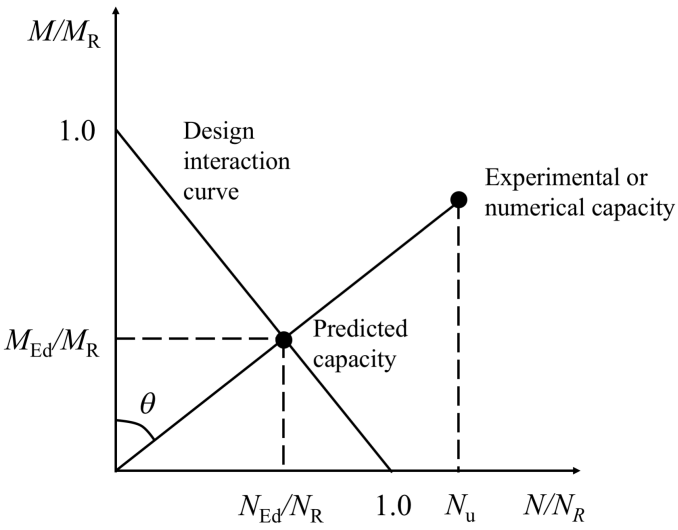

Figure 26: Definition of θ on the moment-axial interaction curve.

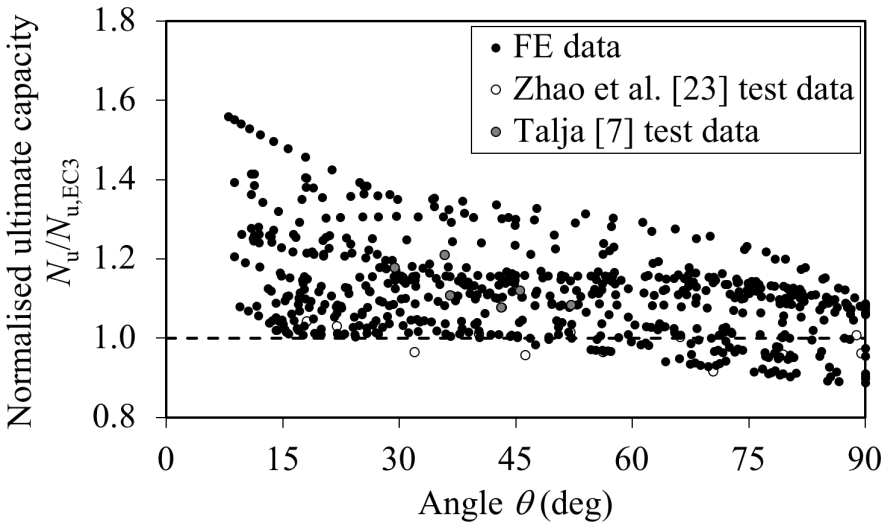

Figure 27: Normalised resistance predictions for the austenitic stainless steel CHS beam-column dataset with the EN 1993-1-4 (2015) approach.

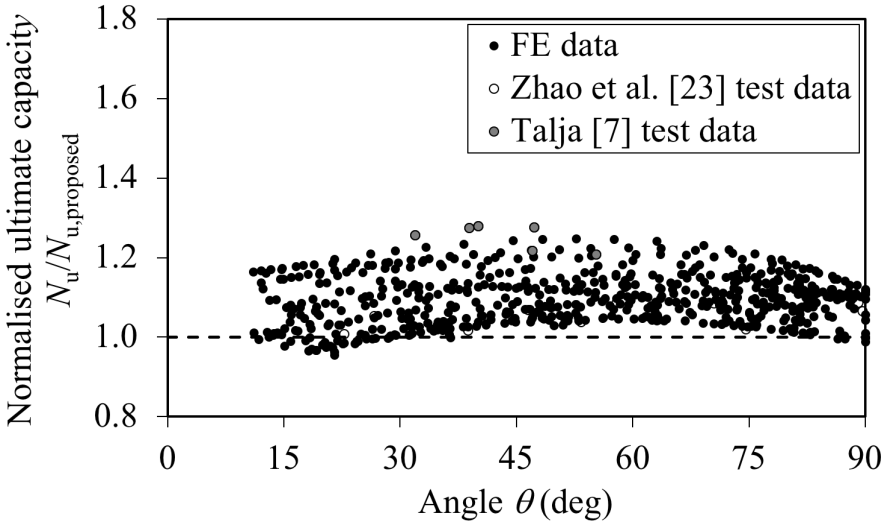

Figure 28: Normalised resistance predictions for the austenitic stainless steel CHS beam-column dataset with the new proposed approach.

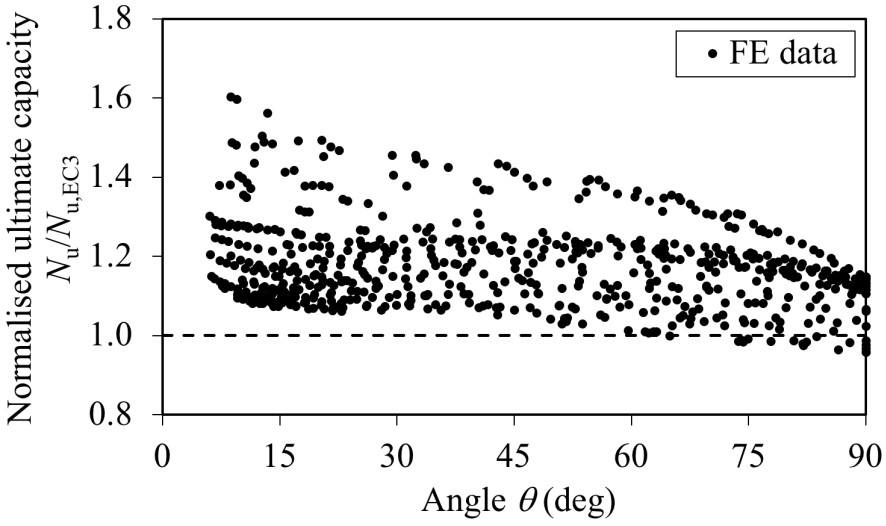

Figure 29: Normalised resistance predictions for the duplex stainless steel CHS beam-column dataset with the EN 1993-1-4 (2015) approach.

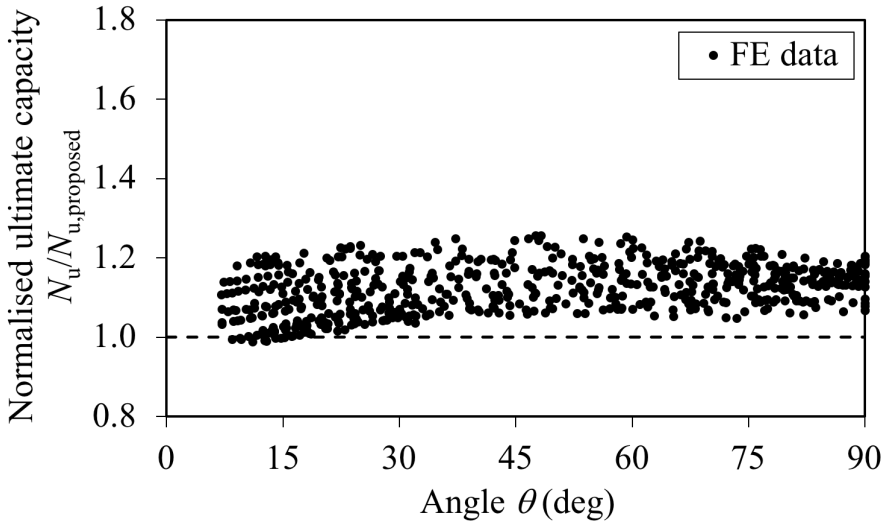

Figure 30: Normalised resistance predictions for the duplex stainless steel CHS beam-column dataset with the new proposed approach.

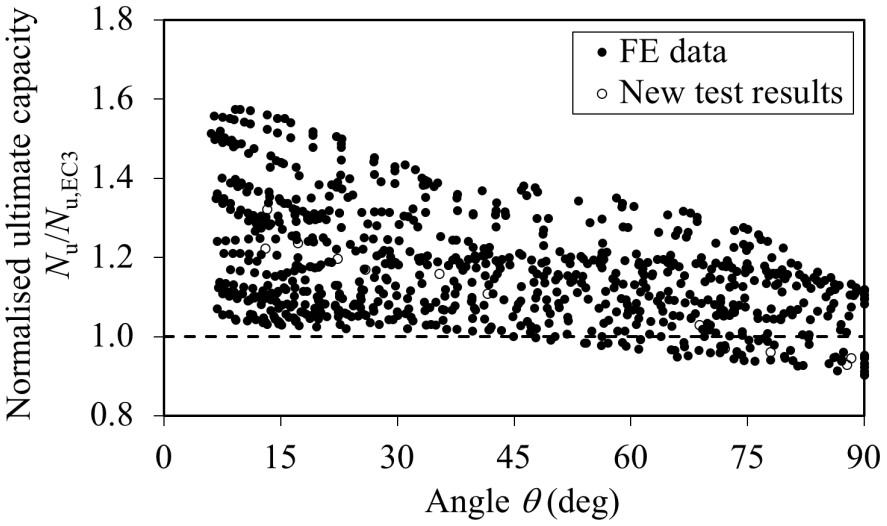

Figure 31: Normalised resistance predictions for the ferritic stainless steel CHS beam-column dataset with the EN 1993-1-4 (2015) approach.

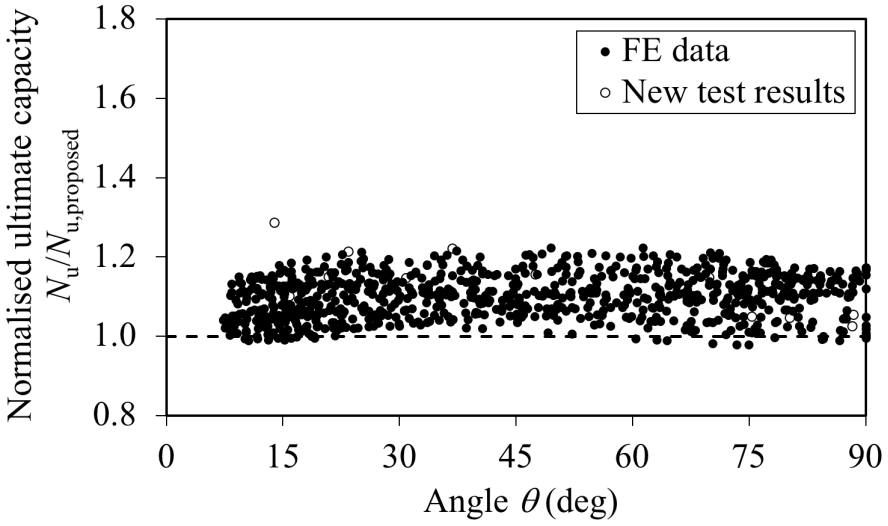

Figure 32: Normalised resistance predictions for the ferritic stainless steel CHS beam-column dataset with the new proposed approach.

results with higher failure loads [71].

For the existing EN 1993-1-4 (2015) CHS beam-column design approach, the target value of the partial safety factor (i.e. $\gamma_{M1} = 1.1$, as recommended in the current code) is attained for the austenitic stainless steel dataset only, while the duplex and ferritic stainless steel datasets have required partial safety factors in excess of $\gamma_{M1} = 1.1$. The new proposal is more consistent across all three types of stainless steel, for the combined test and numerical dataset, with generally lower V_δ values than the EN 1993-1-4 (2015) approach. The required level of reliability is achieved with safety factors lower than the target value of $\gamma_{M1} = 1.1$ for all grades of stainless steel. The proposals made herein are due to be incorporated into the next revision of EN 1993-1-4 (2015), as part of a wider set of improved design rules for stainless steel beam-columns [72].

6. Conclusions

A comprehensive experimental programme focusing upon ferritic stainless steel circular hollow section members under combined axial loading and bending moment has been undertaken. The investigation consisted of material property tests, stub column tests, cross-section level combined axial loading and bending moment tests and member level beam-column tests on ferritic stainless steel CHS. The experimental data were complemented by a pool of finite element results generated through a parallel numerical study. Validated numerical models generated herein have been used to carry out a comprehensive parametric study covering austenitic, duplex and ferritic grades of stainless steel and a wide range of cross-section and member slendernesses and applied loading eccentricities. The ultimate loads were then

Table 17: Summary of statistical analysis results for the EN 1993-1-4 (2015) stainless steel CHS beam-column design approach.

Type	Dataset	n	Over-strength	V_{f_y}	V_{geometry}	$k_{\text{d,n}}$	b	V_δ	γ_{M1}
A	Tests	18	1.3	0.060	0.05	3.09	1.035	0.007	0.95
A	Tests and FE	612	1.3	0.060	0.05	3.09	1.115	0.055	0.93
D	Tests	-	-	-	-	-	-	-	-
D	Tests and FE	621	1.1	0.030	0.05	3.09	1.176	0.049	0.98
F	Tests	12	1.2	0.045	0.05	3.09	1.105	0.009	0.93
F	Tests and FE	813	1.2	0.045	0.05	3.09	1.167	0.073	0.97

Table 18: Summary of statistical analysis results for the new proposed stainless steel CHS beam-column design approach.

Type	Dataset	n	Over-strength	V_{f_y}	V_{geometry}	$k_{\text{d,n}}$	b	V_δ	γ_{M1}
A	Tests	18	1.3	0.060	0.05	3.09	1.119	0.008	0.87
A	Tests and FE	612	1.3	0.060	0.05	3.09	1.096	0.031	0.91
D	Tests	-	-	-	-	-	-	-	-
D	Tests and FE	621	1.1	0.030	0.05	3.09	1.124	0.030	0.99
F	Tests	12	1.2	0.045	0.05	3.09	1.134	0.005	0.90
F	Tests and FE	813	1.2	0.045	0.05	3.09	1.101	0.032	0.95

compared against the current European design guidance and it was observed that the current design approach is conservative at the cross-section level and for members with a high ratio of bending moment to axial load, while it is slightly unconservative for members with a low ratio of bending moment to axial load. A more efficient deformation based design approach, the continuous strength method (CSM), was generally found to offer improvements over the current European guidance at the cross-section level.

New end points for the member level interaction curve were proposed, utilising the more accurate continuous strength method (CSM) bending resistance for the pure bending end point and a new proposed stainless steel CHS flexural buckling curve, that predicts accurate compressive resistances, for the pure compression end point. A new interaction curve was then calibrated to the dataset and was seen to offer more efficient and reliable stainless steel CHS beam-column resistance predictions compared with the EN 1993-1-4 (2015) design approach. The proposed interaction factors can also be conservatively used with the traditional end points.

Statistical analyses were undertaken for both the current EN 1993-1-4 (2015) and new proposed member level design approaches. The existing EN 1993-1-4 (2015) approach requires a slightly higher partial safety factor than the target value of $\gamma_{M1} = 1.1$ for the duplex and ferritic stainless steel datasets, while the new proposals were found to satisfy the reliability requirements with $\gamma_{M1} = 1.1$ for all types of stainless steel.

7. Acknowledgements

This experimental programme was possible thanks to funding and support from the Outokumpu Research Foundation, Engineering and Physical Sciences Research Council (EPSRC), the Ministerio de Economía y Competitividad (Spanish Ministry of Economics and Competitiveness) under the Project BIA 2012-36373 and an Erasmus+ Traineeship grant. The authors would like to acknowledge the contribution of Gordon Herbert, Hayden Spektor and Joel Thomas at Imperial College London and Tomás García, Jordi Lafuente and Jordi Cabrerizo at Universitat Politècnica de Catalunya. The authors would also like to recognise the significant contribution of Itsaso Arrayago in the preparatory work and Rolando Chacón and Enrique Mirambell for their support during the experimental programme.

References

[1] European Committee for Standardisation . EN 1993-1-4:2006+A1:2015 Eurocode 3 - design of steel structures - part 1-4: general rules - supplementary rules for stainless steel. 2015.

[2] European Committee for Standardisation . BS EN 1990:2002+A1:2005 Eurocode - basis of structural design. 2005. ISBN 978 0 580 62664 7. doi:10.1680/cien.144.6.8.40609.

[3] Gardner L. Stability and design of stainless steel structures - Review and outlook. Thin-Walled Structures 2019;141:208–16. doi:10.1016/j.tws.2019.04.019.

[4] SCI . Design manual for structural stainless steel. 4th ed.; Ascot; 2017.

[5] Dutta D. Structures with hollow sections. Weinheim: Wiley VCH; 2002.
[6] Rasmussen KJR, Hancock GJ. Design of cold-formed stainless steel tubular members. I: columns. Journal of Structural Engineering ASCE 1993;119(8):2349–67.
[7] Talja A. Test report on welded I and CHS beams, columns and beam-columns. Report to ECSC VTT Building Technology, Finland 1997;.
[8] Rasmussen KJR. Recent research on stainless steel tubular structures. Journal of Constructional Steel Research 2000;54(1):75–88.
[9] Young B, Hartono W. Compression tests of stainless steel tubular members. Journal of Structural Engineering ASCE 2002;128(6):754–61. doi:10.1061/(ASCE)0733-9445(2002)128:6(754).
[10] Kuwamura H. Local buckling of thin-walled stainless steel members. Steel Structures 2003;3:191–201.
[11] Gardner L, Nethercot DA. Experiments on stainless steel hollow sections - part 1: material and cross-sectional behaviour. Journal of Constructional Steel Research 2004;60(9):1291–318. doi:10.1016/j.jcsr.2003.11.006.
[12] Lam D, Gardner L. Structural design of stainless steel concrete filled columns. Journal of Constructional Steel Research 2008;64(11):1275–82. doi:10.1016/j.jcsr.2008.04.012.
[13] Uy B, Tao Z, Han LH. Behaviour of short and slender concrete-filled stainless steel tubular columns. Journal of Constructional Steel Research 2011;67(3):360–78. doi:10.1016/j.jcsr.2010.10.004.
[14] Zhao O, Gardner L, Young B. Structural performance of stainless steel circular hollow sections under combined axial load and bending - part 1: experiments and numerical modelling. Thin-Walled Structures 2015;101:231–9. doi:10.1016/j.tws.2015.12.003.
[15] Buchanan C, Real E, Gardner L. Testing, simulation and design of cold-formed stainless steel CHS columns. Thin-Walled Structures 2018;130:297–312.
[16] Bardi FC, Kyriakides S. Plastic buckling of circular tubes under axial compression - part I: experiments. International Journal of Mechanical Sciences 2006;48(8):830–41. doi:10.1016/j.ijmecsci.2006.03.005.
[17] Paquette JA, Kyriakides S. Plastic buckling of tubes under axial compression and internal pressure. International Journal of Mechanical Sciences 2006;48(8):855–67. doi:10.1016/j.ijmecsci.2006.03.003.
[18] Stangenberg H. Report to the ECSC - draft final report ferritic stainless steels. Tech. Rep.; RWTH; 2000.
[19] Rasmussen KJR, Hancock GJ. Design of cold-formed stainless steel tubular members. II: beams. Journal of Structural Engineering ASCE 1993;119(8):2368–86.
[20] Burgan BA, Baddoo NR, Gilsenan KA. Structural design of stainless steel members - comparison between Eurocode 3, Part 1.4 and test results. Journal of Constructional Steel Research 2000;54(1):51–73. doi:10.1016/S0143-974X(99)00055-3.
[21] Kiymaz G. Strength and stability criteria for thin-walled stainless steel circular hollow section members under bending. Thin-Walled Structures 2005;43(10):1534–49. doi:10.1016/j.tws.2005.06.006.
[22] Buchanan C, Gardner L, Liew A. The continuous strength method for the design of circular hollow sections. Journal of Constructional Steel Research 2016;118:207–16. doi:10.1016/j.jcsr.2015.11.006.
[23] Zhao O, Gardner L, Young B. Testing and numerical modelling of austenitic stainless steel CHS beam-columns. Engineering Structures 2016;111:263–74. doi:10.1017/CBO9781107415324.004. arXiv:arXiv:1011.1669v3.
[24] Rasmussen KJR, Rondal J. Column curves for stainless steel alloys. Journal of Constructional Steel Research 2000;54:89–107. doi:10.1016/S0143-974X(99)00095-4.
[25] Theofanous M, Chan TM, Gardner L. Structural response of stainless steel oval hollow section compression members. Engineering Structures 2009;31(4):922–34. doi:10.1016/j.engstruct.2008.12.002.
[26] Afshan S, Zhao O, Gardner L. Standardised material properties for numerical parametric studies of stainless steel structures and buckling curves for tubular columns. Journal of Constructional Steel Research 2018;(2017). doi:10.1016/j.jcsr.2018.02.019.
[27] Zhao O, Gardner L, Young B. Structural performance of stainless steel circular hollow sections under

combined axial load and bending - part 2: parametric studies and design. Thin-Walled Structures 2015;101:240–8. doi:10.1016/j.tws.2015.12.005.

[28] Zhao O, Rossi B, Gardner L, Young B. Experimental and numerical studies of ferritic stainless steel tubular cross sections under combined compression and bending. Journal of Structural Engineering ASCE 2015;142(2). doi:10.1061/(ASCE)ST.1943-541X.0001366.

[29] Arrayago I, Real E. Experimental study on ferritic stainless steel RHS and SHS cross-sectional resistance under combined loading. Structures 2015;4:69–79. doi:10.1016/j.istruc.2015.10.003.

[30] Talja A, Salmi P. Design of stainless steel RHS beams, columns and beam-columns. Tech. Rep.; VTT; 1995.

[31] Lui WM, Ashraf M, Young B. Tests of cold-formed duplex stainless steel SHS beam-columns. Engineering Structures 2014;74:111–21. doi:10.1016/j.engstruct.2014.05.009.

[32] Huang Y, Young B. Experimental investigation of cold-formed lean duplex stainless steel beam-columns. Thin-Walled Structures 2014;76:105–17. doi:10.1016/j.tws.2013.11.006.

[33] Zhao O, Gardner L, Young B. Buckling of ferritic stainless steel members under combined axial compression and bending. Journal of Constructional Steel Research 2016;117:35–48. doi:10.1016/j.jcsr.2015.10.003.

[34] Arrayago I, Real E, Mirambell E. Experimental study on ferritic stainless steel RHS and SHS beam-columns. Thin-Walled Structures 2016;100:93–104. doi:10.1016/j.tws.2015.12.004.

[35] Zhao O, Gardner L, Young B. Behaviour and design of stainless steel SHS and RHS beam-columns. Thin-Walled Structures 2016;106:330–45. doi:10.1016/j.tws.2016.04.018.

[36] Chen J, Huang Y, Young B. Design of austenitic and duplex stainless steel SHS and RHS. Journal of Constructional Steel Research 2019;152:143–53. doi:10.1016/j.jcsr.2018.07.003.

[37] Ramberg W, Osgood WR. Description of stress-strain curves by three parameters. 1943. ISBN NACA-TN-902.

[38] Mirambell E, Real E. On the calculation of deflections in structural stainless steel beams: an experimental and numerical investigation. Journal of Constructional Steel Research 2000;54(1):109–33. doi:10.1016/S0143-974X(99)00051-6.

[39] Rasmussen KJR. Full-range stress-strain curves for stainless steel alloys. Journal of Constructional Steel Research 2003;59(2003):47–61.

[40] Gardner L, Ashraf M. Structural design for non-linear metallic materials. Engineering Structures 2006;28(6):926–34. doi:10.1016/j.engstruct.2005.11.001.

[41] Arrayago I, Real E, Gardner L. Description of stress-strain curves for stainless steel alloys. Materials & Design 2015;87:540–52. doi:10.1016/j.matdes.2015.08.001.

[42] European Committee for Standardisation . BS EN 10219-2:2006 Cold formed welded structural hollow sections of non-alloy and fine grain steels. Part 2: tolerances, dimensions and sectional properties; vol. 3. 2006.

[43] Centre for Advanced Structural Engineering . Compression tests of stainless steel tubular columns. Investigation report S770. 1990.

[44] Chan TM, Gardner L. Compressive resistance of hot-rolled elliptical hollow sections. Engineering Structures 2008;30(2):522–32. doi:10.1016/j.engstruct.2007.04.019.

[45] British Standards Institution . BS 5950-1:2000 structural use of steelwork in building - part 1: code of practice for design - rolled and welded sections. 2000.

[46] Zhao O, Rossi B, Gardner L, Young B. Behaviour of structural stainless steel cross-sections under combined loading - part I: experimental study. Engineering Structures 2015;89:236–46. doi:10.1016/j.engstruct.2014.11.014.

[47] Dassault Systèmes Simulia Corp. . Abaqus/CAE 2016. 2015.

[48] Gardner L, Nethercot DA. Numerical modeling of stainless steel structural components - a consistent approach. Journal of Structural Engineering ASCE 2004;130(10):1586–601. doi:10.1061/(ASCE)0733-9445(2004)130:10(1586).

[49] Silvestre N. Generalised beam theory to analyse the buckling behaviour of circular cylindrical shells and tubes. Thin-Walled Structures 2007;45(2):185–98. doi:10.1016/j.tws.2007.02.001.

[50] Rotter JM, Sadowski AJ, Chen L. Nonlinear stability of thin elastic cylinders of different length under global bending. International Journal of Solids and Structures 2014;51(15-16):2826–39. doi:10.1016/j.ijsolstr.2014.04.002.

[51] Buchanan C. Testing and design of conventional and novel stainless steel hollow structural sections. Ph.D. thesis; Imperial College London; 2017.

[52] Gardner L. The use of stainless steel in structures. Progress in Structural Engineering and Materials 2005;7(2):45–55. doi:10.1002/pse.190.

[53] Ashraf M, Gardner L, Nethercot DA. Finite element modelling of structural stainless steel cross-sections. Thin-Walled Structures 2006;44(10):1048–62. doi:10.1016/j.tws.2006.10.010.

[54] Bu Y, Gardner L. Local stability of laser-welded stainless steel I-sections in bending. Journal of Constructional Steel Research 2018;148:49–64. doi:10.1016/j.jcsr.2018.05.010.

[55] Cruise RB, Gardner L. Residual stress analysis of structural stainless steel sections. Journal of Constructional Steel Research 2008;64(3):352–66. doi:10.1016/j.jcsr.2007.08.001.

[56] European Committee for Standardisation . EN 1993-1-1:2005+A1:2014 Eurocode 3: design of steel structures - part 1-1: general rules and rules for buildings. 2014.

[57] Gardner L, Chan TM, Abela JM. Structural behaviour of elliptical hollow sections under combined compression and uniaxial bending. Advanced Steel Construction 2011;7(1):86–112.

[58] Afshan S, Gardner L. The continuous strength method for structural stainless steel design. Thin-Walled Structures 2013;68:42–9. doi:10.1016/j.tws.2013.02.011.

[59] Bock M, Gardner L, Real E. Material and local buckling response of ferritic stainless steel sections. Thin-Walled Structures 2015;89:131–41. doi:10.1016/j.tws.2014.12.012.

[60] Rondal J, Würker K, Dutta D, Wardenier J, Yeomans N. Structural stability of hollow sections. 1st ed.; Verlag TÜV Rheinland; 1992.

[61] Young B, Ellobody E. Column design of cold-formed stainless steel slender circular hollow sections. Steel and Composite Structures 2006;6(4):285–302.

[62] Ellobody E, Young B. Investigation of cold-formed stainless steel non-slender circular hollow section columns. Steel and Composite Structures 2007;7(4):321–37.

[63] Ashraf M, Gardner L, Nethercot DA. Resistance of stainless steel CHS columns based on cross-section deformation capacity. Journal of Constructional Steel Research 2008;64(9):962–70. doi:10.1016/j.jcsr.2007.10.010.

[64] Shu G, Zheng B, Xin L. A new design method for stainless steel columns subjected to flexural buckling. Thin-Walled Structures 2014;83:43–51. doi:10.1016/j.tws.2014.01.018.

[65] Greiner R, Lindner J. Interaction formulae for members subjected to bending and axial compression in Eurocode 3 - the method 2 approach. Journal of Constructional Steel Research 2006;62(8):757–70. doi:10.1016/j.jcsr.2005.11.018.

[66] Boissonnade N, Greiner R, Jaspart JP, Lindner J. Rules for member stability in EN 1993-1-1: background documentation and design guidelines. Tech. Rep.; ECCS European Convention for Constructional Steelwork; New York; 2006.

[67] Greiner R, Kettler M. Interaction of bending and axial compression of stainless steel members. Journal of Constructional Steel Research 2008;64(11):1217–24. doi:10.1016/j.jcsr.2008.05.008.

[68] American Society of Civil Engineers . Specification for the design of cold-formed stainless steel structural members [SEI/ASCE 8-02], [Standards No. 02-008]. New York; 2002.

[69] Standards Australia . Cold-formed stainless steel structures Australian/ New Zealand Standard AS/NZS 4673:2001. 2001.

[70] Afshan S, Francis P, Baddoo NR, Gardner L. Reliability analysis of structural stainless steel design provisions. Journal of Constructional Steel Research 2015;114:293–304.

[71] Bu Y, Gardner L. Laser-welded stainless steel I-section beam-columns: Testing, simulation and design. Engineering Structures 2019;179:23–36. doi:10.1016/j.engstruct.2018.09.075.

[72] Kucukler M, Gardner L, Bu Y. Flexural-torsional buckling of stainless steel I-section beam-columns: Testing, numerical modelling and design. Thin-Walled Structures (in press);XX:xxxxx.